universität wien

MASTERARBEIT / MASTER'S THESIS

Titel der Masterarbeit / Title of the Master's Thesis

„Studying the Climate of Circumbinary Planets“

verfasst von / submitted by

Johannes Mayer BSc BSc MSc

angestrebter akademischer Grad / in partial fulfilment of the requirements for the degree of

Master of Science (MSc)

Wien, 2021 / Vienna, 2021

Studienkennzahl lt. Studienblatt / degree programme code as it appears on the student record sheet:	UA 066 910
Studienrichtung lt. Studienblatt / degree programme as it appears on the student record sheet:	Masterstudium Computational Science
Betreut von / Supervisor:	Univ.-Prof. Dipl.-Phys. Dr. Manuel Güdel
Mitbetreut von / Co-Supervisor:	DEA Dr. Nicolas Iro

Abstract

In recent decades, general circulation models are extensively used to simulate extrasolar planets providing information about their climate, climate variability, and habitability. Together with the finding of planets orbiting binary stars, completely new prospects in searching habitable life are opened up. In this thesis, I present a modified version of the Planet Simulator climate model from the University of Hamburg allowing to simulate the climate of circumbinary planets. For that, an additional module is implemented which numerically integrates the motion of a binary using a semi-implicit Euler scheme. The total solar insolation at the top of the atmosphere is then calculated using simple geometrical considerations. Moreover, I present simulations of an fictitious Earth-like circumbinary aqua-planet in the Kepler-35, Kepler-1647, and Kepler-47 system, and examine its climate and climate variability. I also present new estimates for the habitable zone limits of these systems and provide an extensive comparison with results from the literature. Furthermore, simulations of a circumbinary desert planet are performed and results are compared with those for the aqua-planet. Limitations of the modified Planet Simulator are discussed as well.

I find that the inferred habitable zone limits of the three systems agree reasonably well with those derived from more complex climate models as well as from analytic calculations. While the temporal variability of the climate heavily depends on the variability of the total solar insolation and planetary semi-major axis, mean climatic states of the examined planets are Earth-like and very similar among the three systems. Furthermore, the simulations have shown that the habitable zone of a desert planet is substantially wider than that from an analogous aqua-planet, which is in good agreement with results from the literature.

Zusammenfassung

In den letzten Jahrzehnten werden vermehrt Klimamodelle verwendet, um extrasolare Planeten zu simulieren, welche Informationen zu Klima, Klimavariabilität und Habitabilität liefern. Zusammen mit der Entdeckung von Planeten in Doppelsternsystemen ergeben sich völlig neue Möglichkeiten für die Suche nach extraterrestrischen Leben. In dieser Arbeit wird eine modifizierte Version des Planet Simulator, ein Klimamodell der Universität Hamburg, präsentiert, mit der es möglich ist, das Klima zirkumbinärer Planeten zu simulieren. Hierfür wird ein zusätzliches Modul implementiert, welches die Bewegung des Doppelsterns mittels semi-impliziten Euler-Verfahren integriert und anschließend die Gesamteinstrahlung der beiden Sterne unter Verwendung einfacher geometrischer Überlegungen berechnet. Mit dem modifizierten Klimamodell wird ein fiktiver erdähnlicher Aqua-Planet in den zirkumbinären Systemen Kepler-35, Kepler-1647 und Kepler-47 simuliert und dessen Klima und Klimavariabilität untersucht. Des Weiteren werden neue Schätzungen für die Grenzen der habitablen Zone der drei Systeme präsentiert und ein umfassender Vergleich mit der Literatur durchgeführt. Außerdem werden Ergebnisse von Simulationen mit einem Wüstenplanet präsentiert und mit denen des Aqua-Planeten verglichen. Limitierungen des modifizierten Klimamodells werden ebenfalls diskutiert.
Die Resultate zeigen, dass die neuen Grenzen der habitablen Zone der drei Systeme relativ gut mit denen übereinstimmen, die aus komplexeren Klimamodellen sowie aus analytischen Berechnungen abgeleitet wurden. Des Weiteren wird gezeigt, dass die zeitliche Variabilität des Klimas stark von der Variabilität der Gesamteinstrahlung und der großen Halbachse des Planeten abhängt. Die mittleren Klimazustände der untersuchten Planeten sind hingegen erdähnlich und in allen drei Systemen sehr ähnlich. Darüber hinaus haben die Simulationen des Wüstenplanets gezeigt, dass dessen habitable Zone wesentlich breiter ist als die eines analogen Aqua-Planeten.

Contents

1 Introduction

1.1 Historical Review

The existence of extrasolar worlds was already brought into question by many ancient philosophers more than 2000 years ago. While Aristotle (384-322 B.C.) claimed that no other world than ours exist, Democritus (460-370 B.C.) and Epicurus (341-270 B.C) believed in an infinite number of worlds (Perryman 2011). During this time, only the five innermost planets of our solar system were known as '*wanderers*', from which the word *planet* was derived. First documented attempts to observe extrasolar planets, or exoplanets, were made by the dutch mathematician and astronomer Christiaan Huygens (1629-1695) in the 17th century (Cosmotheoros, 1698). However, observations of exoplanets succeeded for the first time just towards the end of the 20th century, when observational techniques such as radial velocity measurements were accurate enough to detect planet-sized bodies beyond the solar system (Perryman 2011).

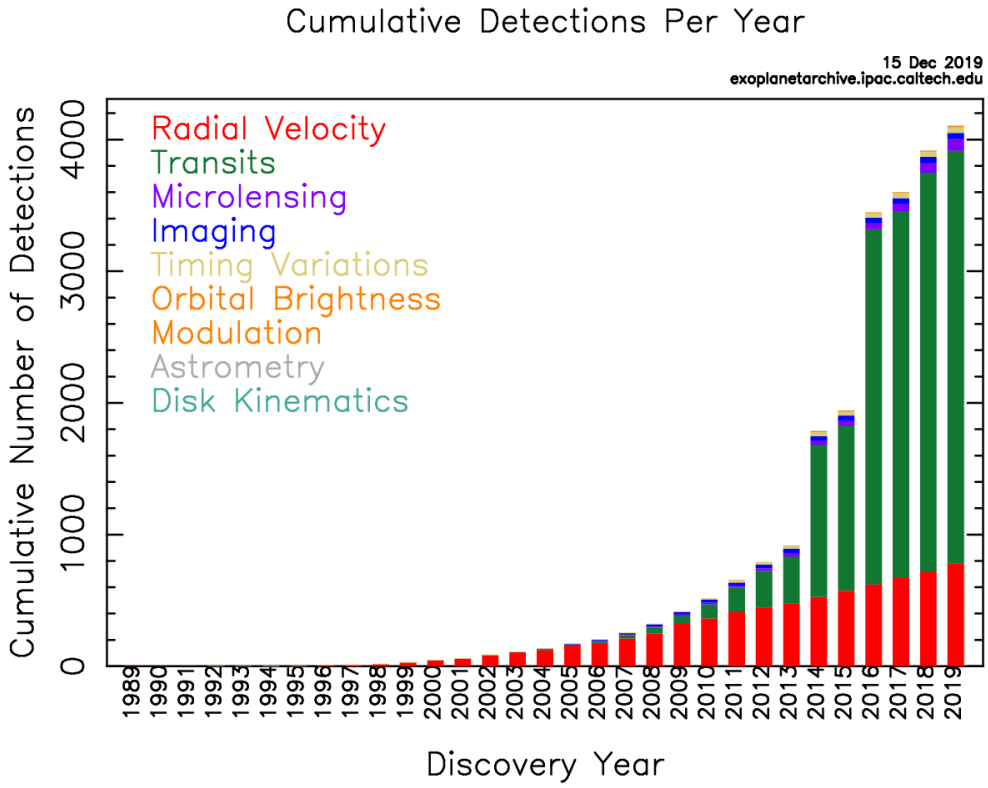

Figure 1: Cumulative exoplanet detections by the discovery year, from the NASA Exoplanet Archive[1]. The colors indicate the number of detected exoplanets by a specific detection method. An explanation of different detection methods can be found elsewhere.

The discovery of the first extrasolar planet in 1992, a planetary system orbiting the pulsar PSR 1257+12 (Wolszczan and Frail 1992), has opened a completely new field of research. Since then, the number of observed exoplanets increases steadily, as

shown in Fig. 1. As of 15 December 2019, a total number of 4104 exoplanets in 3047 planetary systems are confirmed by the National Aeronautics and Space Administration's exoplanet archive[1]. In 1995, the first exoplanet orbiting a main-sequence star, 51 Pegasi b, was detected by Mayor and Queloz (1995) using high-accurate radial velocity measurements. The two Swiss astronomers have recently been awarded with a Noble prize in physics for this discovery underlining the importance of this observation. In 2005, the first planet orbiting a binary system of main-sequence stars (HD 202206 c; Correia et al. 2005) was found – a type of system attractive to search for habitable planets. Seven years later the first multi-planet system orbiting a binary star, Kepler-47, was discovered (Orosz et al. 2012). Since then, several other diverse planetary systems around binary stars have been observed raising the question whether these systems are unique and habitable.

1.2 Astrophysical Background

1.2.1 Abundances

Observations have revealed that about 50 % of all Sun-like stars in the solar neighborhood reside in binary or multi-star systems (Duquennoy and Mayor 1991; Raghavan et al. 2010). Moreover, the binary fraction increases with increasing effective temperature and stellar metallicity (Tian et al. 2018) and more massive stars are more likely to have a companion than less massive stars (Raghavan et al. 2010). These results, and the finding of exoplanets in binary systems, indicate that the co-existence of binary stars and extrasolar planets are the rule and not the exception. Thus, planet-hosting binary stars should be considered for diverse exoplanet studies. Nevertheless, catalogues of exoplanets in binary and multi-star systems, such as the Schwarz catalog (Schwarz et al. 2016), list only ∼150 observed planets in such systems suggesting the effect of observational biases.

Indeed, Eggenberger and Udry (2007) and Wright et al. (2012) have shown that there have been historical biases and selection effects bearing down the abundance of observed planets in binary and multi-star systems. Furthermore, discs of matter around binary stars have been observed indirectly (Mathieu et al. 2000) where terrestrial planets may be formed by the accretion of dust and gas (Lissauer 1993; Safronov 1972) and thus are assumed to be common around binary star systems (Quintana et al. 2007). Hence, these systems must be considered when searching for extrasolar planets. While observations clearly reveal the existence of planets in binary and multi-star systems, computer models still struggle to form planets in such an environment due to gravitational perturbations within the protoplanetary disk caused by the companion star (Gyergyovits et al. 2014; Pilat-Lohinger et al. 2019).

[1] https://exoplanetarchive.ipac.caltech.edu

1.2.2 Types of Planetary Motion

Planets in binary star systems have been observed in two configurations. First, the planet can orbit only one star such that its semi-major axis a_p is smaller than that of the binary a_b. These types of planets are called circumstellar planets, or satellite-type (s-type; Dvorak 1986) and are depicted on the left side of Fig. 2. The planet can either orbit the more massive primary star, known as circumprimary planet, or the less massive secondary star (circumsecondary planet). The second type is known as circumbinary planet, or p-type (planet-type; Dvorak 1986), and is shown on the right side of Fig. 2. In this case, the planet orbits the barycenter of the binary on a much larger separation, such that $a_p > a_b$. Circumstellar discoveries are more frequent at a rate ∼5:1, but observations of circumbinary planets are still in their early stages such that this rate is not meaningful (Martin 2018). Instead, Armstrong et al. (2014) showed that the occurrence rate of coplanar circumbinary planets is similar to that of planets orbiting single stars.

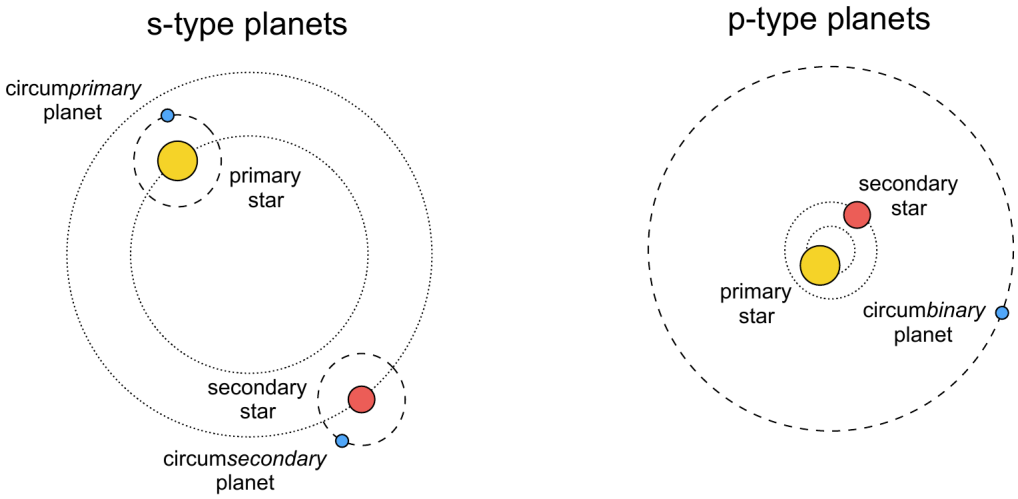

Figure 2: Planetary motion types, from Martin (2018). The figure on the left side illustrates s-type planets with circumprimary planets orbiting the heavier primary star (yellow), and circumsecondary planets orbiting the lighter secondary star (red). The right side illustrates the orbit of p-types, where the planet orbits both stars.

1.2.3 Habitability

From a general point of view, a planet is said to be habitable if reasonable amount of liquid water is available on its surface. However, this is a necessary but not sufficient condition for an eviroment to support life, as various other factors play an important role as well (Hays et al. 2017). In the past, Huang (1959) linked habitability of a planet to its received stellar insolation and introduced the term "*habitable zone*" (HZ) of a main-sequence star. A planet would be in the HZ if the received insolation is similar to Earth's insolation. Thus, the position of the HZ in a single star system strongly depends on the spectral type of the host star (Huang 1959). Later on, Hart (1979) also considered the stellar evolution in the calculation of the

HZ and denoted the corresponding region as *continuously habitable zone*. Based on this work, Kasting et al. (1993) published new estimates for the HZ limits of main-sequence stars by considering the greenhouse effect of atmospheric CO_2 and water vapor. In more recent studies, one-dimensional cloud-free climate models are considered to determine the habitable zone around main-sequence stars (see, e.g., Kopparapu et al. (2014) and references therein).

Under certain conditions, habitability is also possible in binary and multiple star systems. However, the HZ of a binary system can differ from that of a single star, and traditional definitions can only be applied to some extent. In general, the largest differences can be found along the connecting line of the two stars (Pilat-Lohinger et al. 2019). In s-type systems, the planet's insolation is strongly affected by the secondary (and so is the HZ) if it is a close binary, whereas in a wide binary the impact of the secondary is negligible and the HZ is comparable to that of a single star. In p-type systems, the opposite is true. The insolation can be approximated by a single star if it is a close binary (relative to the planet's orbit) and the secondary star is faint. In wide binaries, the insolation differs from that of a single star and the HZ limits must be inferred elsewhere.

There are several numerical and analytic methods to calculate the HZ limits of a binary system. Similar to the HZ in a single star system, Huang (1960) investigated the HZ limits in binaries with the same spectral type. In more recent studies (see, e.g., Eggl et al. (2012), Kaltenegger and Haghighipour (2013), and Haghighipour and Kaltenegger (2013)), this approach has been improved by introducing spectral weights for each binary component so that stars with different spectral types can be considered. The inferred HZ limits are then for a certain amount of total binary insolation such that the climate of the planet remains in a stable condition (see further below). This region is referred to as the *isophote-based habitable zone* (Pilat-Lohinger et al. 2019). However, the climate system has the ability to buffer rapid changes of incoming energy effecting the habitability of a planet drastically, and thus also the HZ limits. For that, Eggl et al. (2012) introduced three new types of habitable zones that are applicable to both s-type and p-type systems (see also Pilat-Lohinger et al. (2019)). First, in the permanently habitable zone (PHZ) the varying binary insolation never exceeds the insolation limits for a planet to be habitable. This type of habitable zone is suitable for planets with a climate very sensitive to changes in insolation. Second, the extended habitable zone (EHZ) is wider than the PHZ and defines a region where the insolation is most of the time within the PHZ limits, but occasionally exceeds them for a short period of time due to the planetary eccentricity. Third, the averaged habitable zone (AHZ) can be used for planets able to buffer large changes in insolation such that only the time-averaged insolation must stay within the limits of the PHZ. Consequently, it is necessary to investigate the climate and interior structure of such planets in order to infer their habitability.

1.2.4 Stability

The dynamical stability is a fundamental property for planets to be habitable. Perturbations and orbital resonances can influence the motion of planets and thus can effect their habitability or even make them unhabitable. First evaluations of the dynamical stability were already performed in the 1970s and 1980s (see e.g., Dvorak 1986; Harrington 1975; Harrington 1977; Szebehely 1980), many years before the first exoplanets were discovered and simulations were severely limited by the sparse computing power. The general approach to detect unstable regions in the parameter space is to run N-body simulations of several massless bodies with different initial conditions determining an inner stability limit for p-types and an outer limit for s-types. That is, planetary orbits in a p-type configuration are stable beyond their stability limit, while s-types are stable within their stability limit. Empirical stability limits were derived by Holman and Wiegert (1999) and Rabl and Dvorak (1988) in this way, which solely depend on the mass ratio and eccentricity of the binary. They showed that the stability region for p-types (s-types) increases (decreases) if the eccentricity and mass-ratio of the binary increases, and that the effect of the eccentricity is stronger than that of the mass-ratio. More recent studies have also considered the eccentricity and inclination of the planet showing that the stable zones are reduced if the eccentricity of the planet is increased, and that the inclination of the planet has no significant effect on the stability (Pilat-Lohinger et al. 2003; Pilat-Lohinger and Dvorak 2002).

1.2.5 Climate Modelling

We have seen that the climate and water content of a planet play a major role in determining the HZ limits of a planet (e.g., see Wolf et al. 2017, and references incorporated therein). Most recently, general circulation models (GCMs) are used to investigate the climate and HZ limits of extrasolar planets (e.g., Way et al. 2018, Cukier et al. 2019, Moorman et al. 2019, and references therein). GCMs are climate models based on hydrodynamical equations originally used to model the Earth's climate. Climate models exist in very different forms and complexity, from primitive 0-dimensional energy balance models (EBMs) to highly complex 3-dimensional ocean-atmosphere coupled GCMs. In general, GCMs consist of multiple modules (e.g., ocean, atmosphere, sea-ice, radiative transfer and vegetation modules) simulating individual parts of the climate system. Climate models of intermediate complexity are usually applied to simulate the climate of exoplanets, where simplified ocean models with a reduced grid resolution or dimensionality are incorporated.

The hydrodynamical equations, or primitive equations, of these climate models consist of the conservation of mass and momentum, the thermodynamical equation, and the equation of state, and are solved on a regular grid to simulate physical processes such as advection and mass and momentum exchange. Other, sub-grid processes (or physically complex processes) such as convection, cloud formation, precipitation, radiation, and turbulence are usually parameterized with empirical equations. These parameterizations vary among different climate models and thus might have an effect on their output.

Important physical processes such as the ice-albedo and water-vapor feedback can already be simulated with simple EBMs, and are crucial mechanisms that can rapidly change the climate and habitability of a planet. The positive ice-albedo feedback process describes the interaction between the reflected radiation of sea ice (or snow) due to its high albedo and the sea ice extent. The process is positive because it amplifies the change, i.e., an increase in the sea ice extent increases the reflected radiation and thus more sea ice can be formed. On the other hand, decreasing the sea ice extent leads to a decrease in reflected radiation, and thus more radiation is absorbed further decreasing the sea ice extent on a planet. Shields et al. (2013) have shown that the ice-albedo effect is stronger for planets orbiting stars with higher near-UV radiation, that is, the sea ice extent is much greater on planets orbiting hotter F-stars than on planets orbiting cooler G-stars at an equivalent flux distance. The water-vapor feedback is also positive and works in a similar way. Saturation vapor pressure increases in a warming atmosphere and thus more water vapor can be hold by the atmosphere. This further warms the atmosphere due to the larger greenhouse effect of water vapor. Another important feedback mechanism comes from the Stefan-Boltzmann law. It acts as a negative feedback process that can stabilize the climate of a planet. According to the Stefan-Boltzmann law, more energy is radiated into space as the temperature of a planet increases, which, as a consequence, cools the planet.

These processes are important and can rapidly change the climate of a planet. A strong ice-albedo effect can lead to the so-called Snowball state where the planet's surface is fully covered by sea ice. On the other hand, a planet will fall into the moist Greenhouse state if its stratospheric water vapor exceeds a mixing ratio of 0.1 % (Kasting 1988; Kasting et al. 1984), which is equivalent to 1 g kg^{-1} specific humidity. In this state the stratospheric water is dissociated by the UV radiation so that the hydrogen and, consequently, the water inventory of the planet is lost to space. Both the moist Greenhouse and the Snowball state depend on the CO_2 concentration of the atmosphere (Wordsworth and Pierrehumbert 2013) and are related to the transition into an uninhabitable planet. Such processes are thus important for the definition of the habitable zone.

While habitability is usually associated with planets possessing abundant liquid water resources (so-called aqua-planets), Abe et al. (2011) used a climate model to show that dry planets (or desert planets) with no oceans and limited amount of liquid water can be habitable as well. They also showed that desert planets have wider habitable zones than conventional aqua-planets. An Earth-sized desert planet with low obliquity could be habitable up to a globally averaged net insolation[2] of 415 W m^{-2} (compared to 330 W m^{-2} for an analogous aqua-planet) due to the weaker Greenhouse effect of the dry atmosphere. In addition, the outer HZ limit is shifted outwards as the lack of large water reservoirs prevents the planet from global freezing (Abe et al. 2011).

[2]The global net insolation is defined as $I = S/4(1-\alpha)$ where S is the total solar insolation (or solar constant) and α is the effective albedo of the planet.

One climate model that is sometimes used to simulate the climate of exoplanets (see e.g., Lucarini et al. 2013, Menou 2013, Abbot et al. 2018, Paradise et al. 2019) is the *Planet Simulator* (PlaSim) developed by the Meteorological Institute at the University of Hamburg (Lunkeit et al. 2004). PlaSim is an open source climate model of intermediate complexity comprising a fully three-dimensional atmospheric model with T21, T31 or T42 horizontal spectral resolution and vertical sigma-coordinates. It is combined with a 0-dimensional ocean model (one level) for the mixed ocean layer, a dynamic vegetation model for non-glaciated land surface grid cells called SimBA, and a sea ice model with a linear temperature gradient in the ice layer as well as no heat storage capacity. The sea ice model is very simplified, e.g., sea ice is formed if the ocean temperature drops below the freezing point, and consists of prognostic variables for the sea ice temperature and thickness. Moreover, sea ice can accumulate snow that change the albedo. Further sea ice processes are described in PlaSim's reference manual (Lunkeit et al. 2004). Other processes, such as surface fluxes, radiation, cloud formation, and convection are parameterized (as mentioned above) and also described in PlaSim's reference manual. PlaSim also provides a graphical interface for convenient handling, post-processing routines to convert the output to widely-used grib and netCDF file formats, and MPI support for parallel execution.

1.2.6 Example: Climate of Kepler-35b

Popp and Eggl (2017) gave a comprehensive example on how the climate of a hypothetical Earth-like aqua-planet in the circumbinary system Kepler-35 can be simulated using the atmospheric GCM ECHAM6 (Stevens et al. 2013). They examined the HZ limits for the aqua-planet and showed that the planet can indeed be habitable. They found an inner limit of 1.165 au (transition to moist Greenhouse state) and an outer limit of 1.195 au (full glaciation) with Earth-like CO_2 concentration.

Figure 3 illustrates the zonal mean of the planet's surface temperature, total cloud cover, effective albedo, and total precipitation in steady state for different planetary semi-major axes. The climate is also simulated for a similar planet in the solar system indicating that the mean climatic state and habitability of the circumbinary planet in the Kepler-35 system is barely affected by the rapid variation of the binary insolation. Popp and Eggl (2017) concluded that such binary star systems are excellent candidates to look for habitable planets, and that climate models are necessary to estimate the climate variation of observed planets.

1.3 Motivation and Research Question

We have seen that planets in binary star systems are not uncommon and can exist in the habitable zone of a binary (e.g., Kepler-47c; Welsh et al. 2014). Unfortunately, none of the observed circumbinary planets are terrestrial leading to the fascinating idea of habitable moons orbiting planets in the habitable zone (Welsh et al. 2014). However, it is only a matter of time until the first terrestrial circumbinary planet

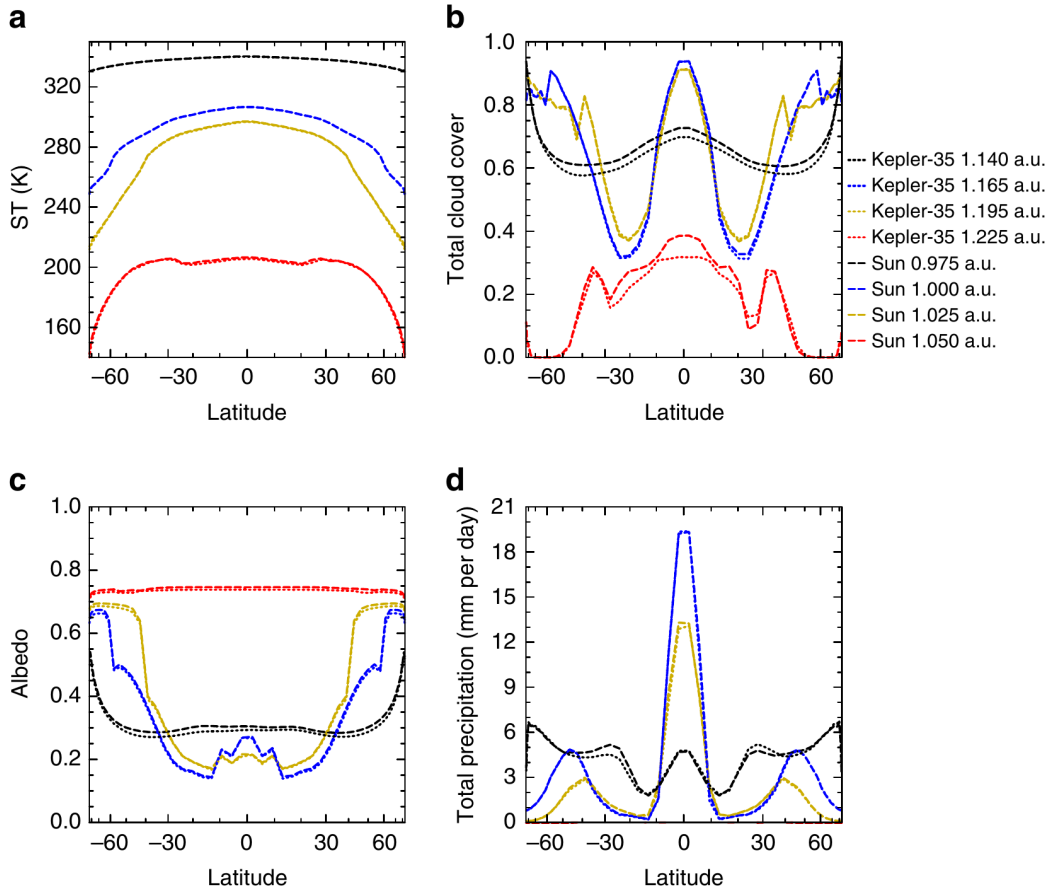

Figure 3: from Popp and Eggl (2017). It shows the zonal-means of the surface temperature (panel a), the total cloud cover (b), the effective albedo (c), and the total precipitation (d). The snowball states are illustrated in red, the moist Greenhouse states in black, and the habitable states in yellow and blue. The fictitious aqua-planet in the Kepler-35 system is illustrated by dotted lines. For comparison, the aqua-planet is also simulated for a Sun-like system (dashed lines). Temporal averages are taken over a period of 10800 Earth-days in steady state.

will be observed. Promising satellite missions for that are the upcoming Plato space telescope[3], the European Extremely Large Telescope[4], and the James Webb Telescope[5]. The fact that we can not directly resolve the atmospheres of exoplanets with current astronomical instruments (both ground-based and space telescopes) yet, suggests the use of climate models to gain an insight into the atmosphere, climate, and habitability of extrasolar planets. These models have demonstrated that circumbinary planets can indeed be habitable. Yet, there are only a few publications investigating the climate of circumbinary planets and additional work has to be done. Thus, it is important to make a further step in that direction with this master thesis.

[3] sci.esa.int/documents/33240/36096/1567260308850-PLATO_Definition_Study_Report_1_2.pdf
[4] www.eso.org/public/archives/brochures/pdf/brochure_0022.pdf
[5] www.jwst.nasa.gov/content/science/origins.html

How does a binary star affect the climate of a planet? For a given circumbinary planet, what are the climatic conditions for habitability? How are the HZ limits influenced by the choice of the climate model? Do we get the same climate states and HZ limits when using different climate models, or do the results differ significantly? In order to answer these questions, I present a modification of the PlaSim climate model allowing to simulate the climate of circumbinary planets. In the first step, a hypothetical water-rich planet in the Kepler-35 system is simulated and results are compared with those from Popp and Eggl (2017). They used a more complex model, which may lead to different habitable zone limits. Additionally, the binary systems Kepler-1647 and Kepler-47 are used to examine the climate and habitability of both desert and water-rich planets. The goal of this thesis is to investigate circumbinary planets with PlaSim and get further insights into their climate and habitability.

This thesis is structured as follows. Section 2 introduces the basic equations that have to be changed in order to consider the binary insolation on a circumbinary planet. Section 3 summarizes the model setup and methodology to infer HZ limits. Results for Kepler-35, Kepler-1647, and Kepler-47 are presented in section 4 and discussed in section 5. The new binary routines and necessary modifications of the PlaSim code are summarized in Appendix A.

2 Implementation of the Binary Star Insolation

This section introduces numerical approaches to compute the binary star insolation in PlaSim. First, section 2.1 summarizes the calculation of the single star insolation as done by PlaSim. The subsequent sections then portray how this approach is modified in order to compute the binary star insolation on a circumbinary planet. Limitations of the modified PlaSim code are summarized in section 2.4.

2.1 How PlaSim works

This section describes how the single star insolation at the top of the atmosphere (TOA) of a planet is calculated in PlaSim. The electromagnetic spectrum is divided into two spectral bands for which particular processes take place (see PlaSim reference manual for further details; Lunkeit et al. 2004). The first band covers ultraviolet and visible wavelengths with $\lambda < 0.75$ μm, the second covers long-wave radiation with $\lambda > 0.75$ μm. The TOA insolation is calculated in the *radmod* module and needs four quantities in total. First, the spectral partitioning values E are needed describing the percentage of electromagnetic energy in each of the aforementioned spectral bands. For a G-type main-sequence star, the default values are $\mathrm{E_{sw}} = 0.517$ and $\mathrm{E_{lw}} = 0.483$. These values are defined in PlaSim's *radmod* module. Furthermore, the computation of the TOA insolation in PlaSim is not based on the distance between planet and host star. Instead, it uses a solar constant $\mathrm{S_0}$ (which implicitly includes the distance) and a normalized planet-star distance (Berger 1978) following

$$\rho = \frac{r}{a} = \frac{1 - e^2}{1 + e \cdot cos(\nu)}, \tag{1}$$

where r is the Euclidean planet-star distance and a is the planetary semi-major axis. Both are not used in PlaSim. Instead, the right side is used, with the planet's orbital eccentricity e (restricted to $\mathrm{e} < 0.1$) and the true anomaly ν. ρ is dimensionless and describes the variation of $\mathrm{S_0}$ during one revolution of the planet. It usually varies between -1.5 and 1.5. The fourth quantitiy is the zenith angle, which is calculated using the declination and hour angle. Based on Berger (1978) the star's declination angle is given by

$$\delta(\lambda_l) = asin(sin(\epsilon) \cdot sin(\lambda_l)), \tag{2}$$

where ϵ is the planet's obliquity, and λ_l is the true longitude of the planet measured from a reference direction. λ_l is related to the true anomaly ν and the longitude of the periapsis $\bar{\omega}$ through $\lambda_l = \nu + \bar{\omega}$. The hour angle is given by

$$h(\lambda, t) = t_{mins} \cdot c_{rad} + \lambda - \pi, \tag{3}$$

where t_{mins} is the current time of a day (converted from minutes to radians by multiplying $c_{rad} = 2\pi/1440$), and λ is the geographical longitude in radians. Thus, the solar zenith angle θ is calculated for each grid point with

$$\theta(\phi, \lambda, \lambda_l, t) = sin(\delta) \cdot sin(\phi) + cos(\phi) \cdot cos(\delta) \cdot cos(h). \tag{4}$$

Here, ϕ is the geographical latitude. The zenith angle is set to zero if it is smaller than a predefined dawn angle simulating the planet's night side. The TOA insolation is then calculated for each spectral band separately using the spectral partitioning values E, solar constant S_0, normalized planet-star distance ρ (Eq. 1), and the solar zenith angle θ (Eq. 4) such that

$$F_{TOA,sw} = E_{sw} \cdot S_0 \cdot \rho^{-2} \cdot \theta(\phi, \lambda) \tag{5}$$
$$F_{TOA,lw} = E_{lw} \cdot S_0 \cdot \rho^{-2} \cdot \theta(\phi, \lambda) \tag{6}$$

where ρ^{-2} is the inverse of the quadratic normalized planet-star distance ρ, which is called the eccentricity factor. F_{TOA} is further used to compute fluxes at layer interfaces. Some variables are read from an input file such that the program does not have to be compiled again. That is, the input for PlaSim to compute the TOA insolation is the eccentricity e, solar constant S_0, obliquity ϵ and the longitude of the periapsis $\bar{\omega}$, which are all read from the file '*planet_namelist*'. Specific values and other variables in this input file are introduced in section 3.

2.2 Computation of the Binary Motion

In order to simulate the binary insolation at the TOA of the planet properly, the motion of the binary has to be simulated. Instead of solving a three-body problem, including the planet and the two stars, only the latter is numerically integrated. That is, the two-body problem is solved, which simplifies the equations of motion and integration of the binary. This is done in additional routines that are implemented (see appendix). The orbital position of the planet is still controlled by PlaSim. We start with Newton's law of gravitation to derive the equations of motion for the primary star. We write

$$F_G = \frac{G \cdot m_1 \cdot m_2 \cdot r}{|r|^3}, \tag{7}$$

where G is the gravitational constant, m_1 and m_2 are the masses of star 1 and 2, and r is the Euclidean distance between them. From Newton's second law of motion we can formulate an equation of motion for the x and y component separately, that is,

$$\frac{dx^2}{dt} = \frac{F_{G,x}}{m_1} \tag{8}$$

$$\frac{dy^2}{dt} = \frac{F_{G,y}}{m_1} \tag{9}$$

where $F_{G,x}$ and $F_{G,y}$ indicate the x- and y-component of the gravitational force F_G. Substituting Eq. (7) into these equations leads to

$$\frac{dv_x}{dt} = -\frac{G \cdot m_2 \cdot x}{|r|^3} \qquad \text{with} \qquad v_x = \frac{dx}{dt} \tag{10}$$

$$\frac{dv_y}{dt} = -\frac{G \cdot m_2 \cdot y}{|r|^3} \qquad \text{with} \qquad v_y = \frac{dy}{dt}. \tag{11}$$

where v_x and v_y are the x- and y-velocities, and r is replaced by their distances x and y, respectively. These differential equations have to be converted into difference equations. Using forward differences and reformulate the equations leads to

$$v_{x,i+1} = v_{x,i} - \Delta t \cdot \frac{G \cdot m_2 \cdot x_i}{|r|^3} \tag{12}$$

$$x_{i+1} = x_i + \Delta t \cdot v_{x,i+1} \tag{13}$$

$$v_{y,i+1} = v_{y,i} - \Delta t \cdot \frac{G \cdot m_2 \cdot y_i}{|r|^3} \tag{14}$$

$$y_{i+1} = y_i + \Delta t \cdot v_{y,i+1} \tag{15}$$

where Δt indicates the time step of the binaries' integration scheme, and the indices i and i+1 denote the previous and current time step, respectively. The equations of motion for the secondary are derived in the same way (with m_1 instead of m_2). Note that in Eq. (13) and (15) the velocities $v_{x,i}$ and $v_{y,i}$ has been replaced by $v_{x,i+1}$ and

$v_{y,i+1}$ leading to the so called semi-implicit Euler (or Symplectic Euler) scheme. This is an one-step method with first-order accuracy and sufficient for the integration of the binary. The integration is performed at the beginning of the climate simulation, with sufficient small time step Δt (e.g., $\sim$225 s) to avoid numerical instabilities such as barycenter drift or numerical precession of the perihelion. Please note that the integration of the binary takes less then a minute to simulate 50 years, while the full climate simulation requires $\sim$2 hours.

In the following, initial positions and velocities for Eqs. (12)–(15) are derived. Note that all three bodies, the two stars and the planet, are initially on the x-axis of the coordinate system (i.e., y = 0). Thus, subsequent velocity terms describe the y-component of the velocity vector and indices with respect the coordinate system are neglected. The initial position of the primary star (index '1') is derived from the center of mass condition

$$m_1 \cdot a_1 = m_2 \cdot a_2, \tag{16}$$

where a_1 and a_2 are the semi-major axes of the two stars. This equation is substituted into a_2 of the binary semi-major axis $a_B = a_1 + a_2$ providing an expression for a_1. This is combined with the definition of the periapsis distance of an ellipse

$$r_1 = a_1 \cdot (1 - e_B), \tag{17}$$

where e_B is the eccentricity of the binary, to obtain the initial x-position of the primary star. Its position vector is thus given by

$$r_{1,x} = a_B \cdot (1 - e_B) \cdot \frac{m_2}{m_1 + m_2}, \tag{18}$$

$$r_{1,y} = 0. \tag{19}$$

where $r_{1,x}$ and $r_{1,y}$ are the x- and y-distance to the center of mass. The initial position of the secondary (indix '2') is motivated by the barycenter equation

$$r_2 = r_{2,x} = r_{bc} \cdot \frac{m_1 + m_2}{m_2} - \frac{m_1}{m_2} \cdot r_1 = -\frac{m_1}{m_2} \cdot r_1, \tag{20}$$

where r_{bc} is the position of the barycenter, or center of mass, which is defined to be at the origin (0,0) of the coordinate system such that r_2 only depends on the mass ratio of the two stars and the initial position of the primary. This is the initial x-position of the secondary, and $r_{2,y} = 0$. Thus, Eqs. (18) and (20) depict the initial positions of the two stars in the periapsis. To infer the initial velocities v_1 and v_2 in the periapsis, the vis-viva equation is used in the form

$$v^2 = GM\left(\frac{2}{r} - \frac{1}{a_B}\right), \tag{21}$$

where v is the relative velocity of the two stars such that $v = v_1$ - v_2, $M = m_1 + m_2$ is the total mass of the binary system, and $r = r_1 + r_2$ is the distance between the two bodies. We can rewrite this equation with the formula of the periapsis distance $r = a_B \cdot (1 - e_B)$ such that

$$v = \sqrt{\frac{GM}{a_B}\frac{(2a_B - r)}{r}} = \sqrt{\frac{GM}{a_B}\frac{2a_B - a_B \cdot (1 - e_B)}{a_B \cdot (1 - e_B)}} = \sqrt{\frac{GM}{a_B}\left(\frac{1 + e_B}{1 - e_B}\right)}. \tag{22}$$

This equation describes the relative velocity of the two stars in the periapsis depending on the total mass and the semi-major axis and eccentricity of the binary. The velocities of the individual stars are derived from the momentum conservation of the barycenter given by

$$m_1 \cdot v_1 + m_2 \cdot v_2 = P_{bc}, \tag{23}$$

where we demand the momentum of barycenter P_{bc} to be zero. That is, the center of mass must be in rest. Reformulating this equation leads to the velocity of the primary star

$$v_1 = -\frac{m_2}{m_1} \cdot v_2 = \frac{m_2}{m_1} \cdot (v - v_1) = \frac{m_2}{m_1 + m_2} \cdot v, \tag{24}$$

which depends on the masses of the binary and the relative velocity formulated in Eq. (22). The velocity of the secondary in the periapsis is then

$$v_2 = -\frac{m_1}{m_2} \cdot v_1 \tag{25}$$

and depends on the mass ratio of the two stars and the velocity of the primary, but with negative sign as this star moves in the opposite direction. Please note that these equations specify only the y-components of the velocity vector, the x-components are zero. The full initial velocity vector of the binary can thus be written as

$$v_{1,x} = 0 \tag{26}$$

$$v_{1,y} = \left(\frac{m_2}{m_1 + m_2}\right) \cdot \sqrt{\frac{G \cdot (m_1 + m_2)}{a_B} \cdot \left(\frac{1 + e_B}{1 - e_B}\right)} \tag{27}$$

$$v_{2,x} = 0 \tag{28}$$

$$v_{2,y} = -\frac{m_1}{m_2} \cdot v_{1,y}. \tag{29}$$

Using the initial periapsis velocities (Eqs. (26)–(29)) and positions (Eqs. (18)–(20)) in combination with a sufficient small step size Δt leads to stable binary orbits around its center of mass, which remains in the origin of the coordinate system. Please note that PlaSim's integration step size of 2700 seconds must be a multiple of the binary step size Δt. That is, if $\Delta t = 225$ seconds, exactly 12 binary integration steps are needed to simulate the motion of the binary for one PlaSim time step. This is important for the correct calculation the binary insolation. An example is given in Fig. 4 showing binary orbits integrated over 160 years. To simulate the binary motion, the eccentricity e_B and semi-major axis a_B of the binary as well as individual stellar masses m_1 and m_2 are needed, which are all read from the newly defined input file '*binary_namelist*'[6]. Other input variables in this file are introduced in section 3.

The conservation of the total orbital energy of the binary star is an important requirement that has to be satisfied by the integration scheme. It is the sum of the kinetic and potential energy such that

$$E = E_{kin} + E_{pot} = \left(\frac{m_1 \cdot v_1^2}{2} + \frac{m_2 \cdot v_2^2}{2}\right) - \frac{G \cdot m_1 \cdot m_2}{r} \tag{30}$$

where E_{kin} is the kinetic energy of both stars. This is an important constraint for the integration scheme to provide stable orbits. As an example, Fig. 5 shows the orbital energy of the Kepler-35 system integrated over a period of 80 years using the aforementioned semi-implicit Euler scheme. The total energy (black line) does not show any drift over the full period of time, but oscillates with an amplitude five orders of magnitude smaller than the mean total energy. Thus, integration with the semi-implicit Euler leads to sufficiently stable orbits.

[6] An example for the input file *binary_namelist* can be found in the appendix or at http://www.mayer.tv/programs/binary_namelist.

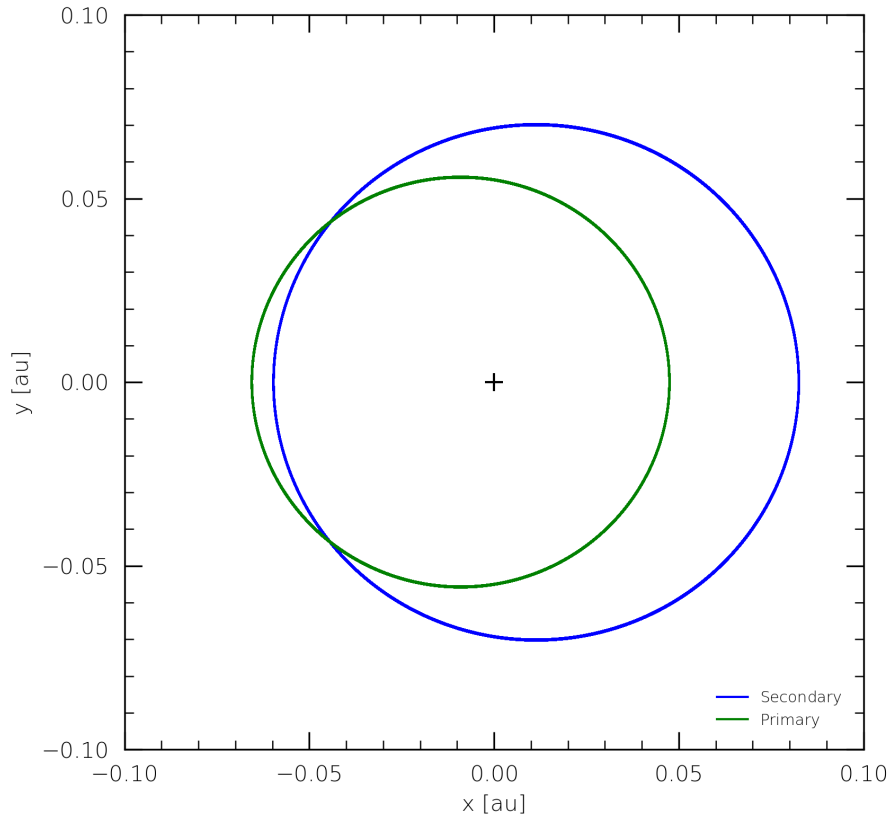

Figure 4: Binary orbits with a small eccentricity integrated over 160 Earth-years, and an integration time step of 225 seconds. The green line indicates the primary and the blue line the secondary. The '+' illustrates the barycenter of the system.

2.3 Computation of the Insolation

In this section, the computation of the binary insolation at the TOA of the circumbinary planet is motivated. For that, Eqs. (2), (3), and (4) are modified and computed for each star separately. In binary simulations, the unmodified equations describe quantities with respect to the barycenter of the binary. That is, the position of the barycenter coincides with position of the central body of single star simulations. To compute δ, h and θ for each star of the binary system, a displacement angle (apparent angle between star and barycenter as seen from the planet) must be added to the barycenter quantities. Thus, the equations for the primary star can be written as

$$\delta_1(\lambda_{bc}, \alpha_{S1P}) = asin(sin(\epsilon) \cdot sin(\lambda_{bc} - \alpha_{S1P})), \tag{31}$$

$$h_1(\lambda, \alpha_{S1P}, t) = t_{mins} \cdot c_{rad} + \lambda - \pi - \alpha_{S1P}, \tag{32}$$

$$\theta_1(\phi, \lambda, \lambda_{bc}, \alpha_{S1P}, t) = sin(\delta_1) \cdot sin(\phi) + cos(\phi) \cdot cos(\delta_1) \cdot cos(h_1), \tag{33}$$

where α_{S1P} is the displacement angle between primary and barycenter as seen from the planet. The same is valid for the secondary using the displacement angle α_{S2P}.

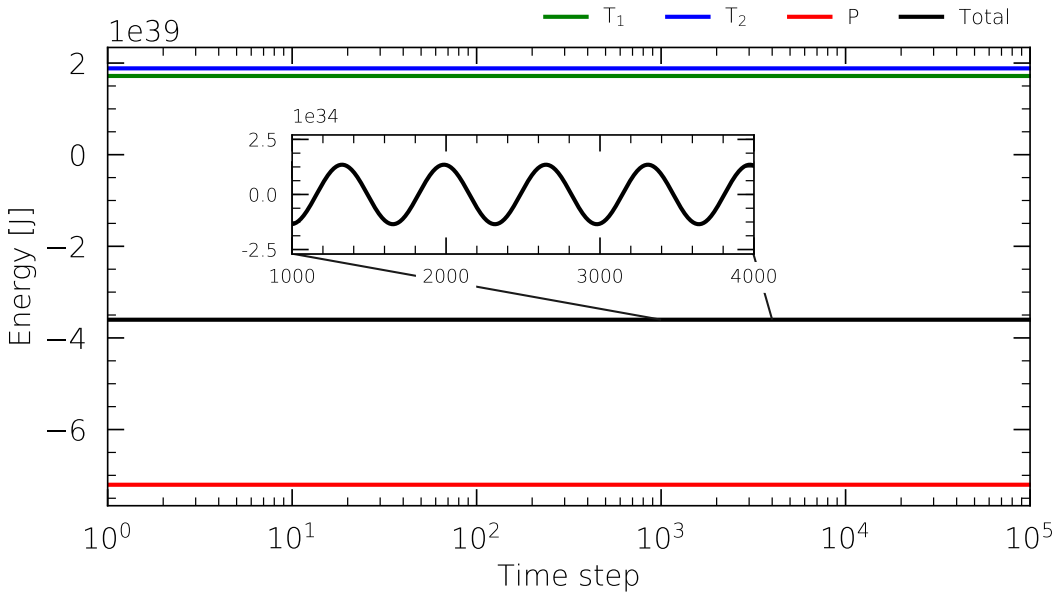

Figure 5: Time series of the orbital energy of Kepler-35 showing the potential energy in red, the kinetic energy of the primary (with subscript 1) and secondary in green and blue, and the total orbital energy in black. The x-axis shows the number of time steps, where one step is equivalent to 2700 seconds. The inset graph emphasizes the total energy, but zero averaged to show its periodic oscillations. However, it does not show any drift and the resulting orbits are stable over the full period of time. Note that the y-axis scaling is five orders of magnitude larger than that of the inset graph.

Figure 6 illustrates the declination, hour angle, and zenith angle of a binary system (according to Eqs. (31)–(33)) as well as of its barycenter (or single star; according to Eqs. (2)–(4)) as seen from a single grid point.

The computation of the TOA insolation is then slightly changed, as described in the following. Instead of reading the solar constant from an input file, an explicit value for the barycenter-planet distance (equivalent to r in Eq. (1)) is allocated and allows to calculate the solar constant as a function of the star's temperature or mass. The former can be used in combination with the Stefan-Boltzmann law, which is given by

$$L_{1,2} = 4\pi R_{1,2}^2 \cdot \sigma T_{1,2}^4, \tag{34}$$

to compute the luminosity of each star separately, where R is the radius and T is the temperature of the respective star. If the individual masses of the binary are known, the mass-luminosity relation

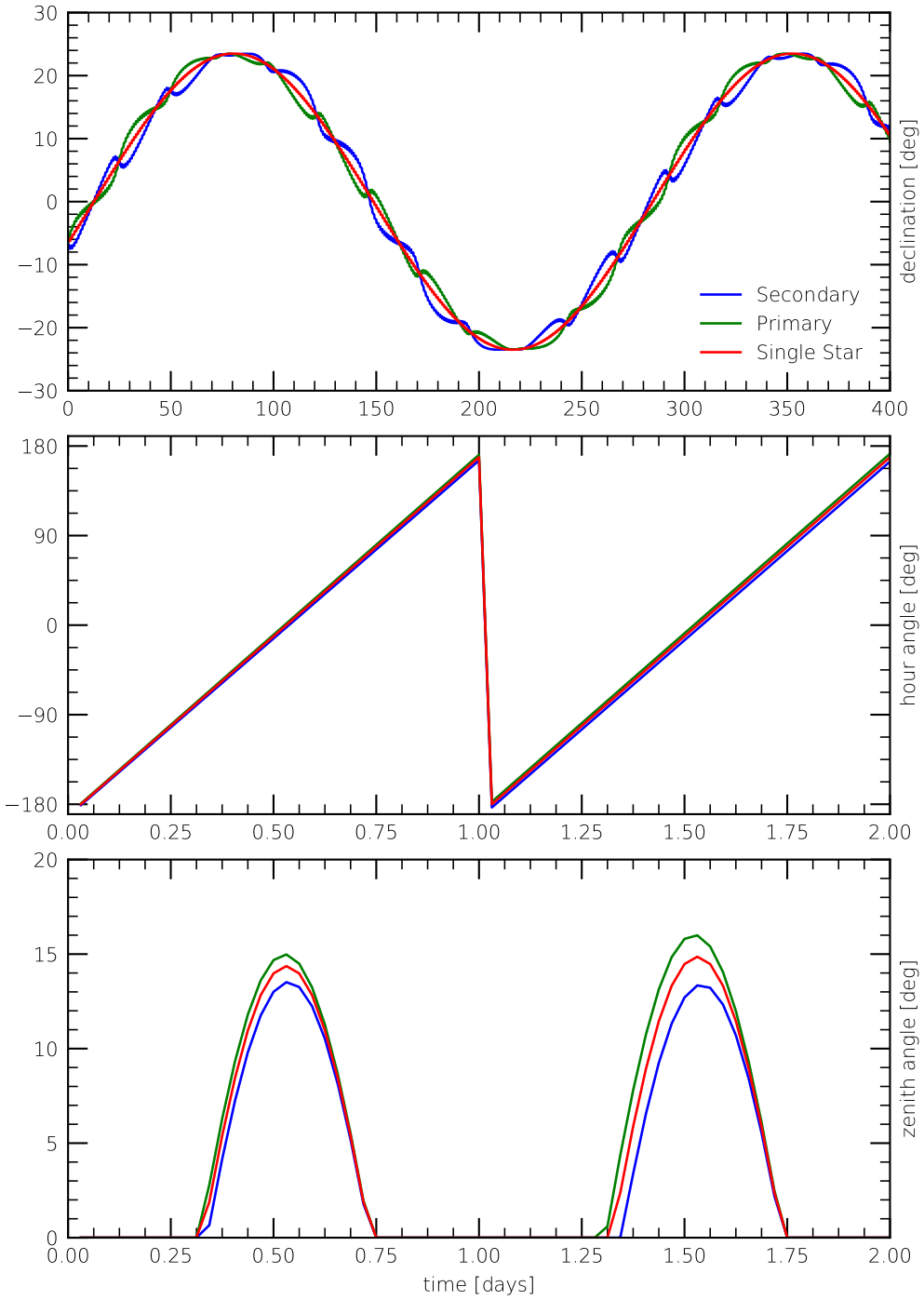

Figure 6: Declination δ, hour angle h, and zenith angle θ of a binary star with masses M = 1.0 and 0.8 $M_\odot$. The quantities are calculated for a single grid point on a planet with obliquity $\Omega = 23.5°$. Green and blue lines are with respect to individual stars of the binary system, and the red line is with respect to the barycenter (or single star). The binary has an eccentricity $e_B = 0.5$ and semi-major axis $a_B = 0.2$ au. The planet has no eccentricity and a semi-major axis $a_P = 1.0$ au. Note that δ is shown for 400 days, while h and θ is shown for only two days.

$$L_{1,2} = L_{\odot} \left(\frac{M_{1,2}}{M_{\odot}} \right)^{\beta_{1,2}} \tag{35}$$

can be used to calculate the star's luminosity, where $\beta_{1,2} = 4$ for main sequence stars with $0.43\ \mathrm{M}_{\odot} < \mathrm{M} < 2.00\ \mathrm{M}_{\odot}$, and $\mathrm{M}_{\odot}$ and $\mathrm{L}_{\odot}$ are the sun's mass and luminosity, respectively. In both cases, the solar constant of each individual star is computed with

$$S_{1,2} = \frac{L_{1,2}}{4\pi r_0^2}, \tag{36}$$

where r_0 is the initial distance between planet and barycenter of the binary, and thus remains constant over the whole integration. Instead, PlaSim's approach is used, where the eccentricity factor describes the temporal variation of the insolation. Thus, we define the eccentricity factor (according to Eq. (1)) of each star to be

$$\rho_{1,2}^{-2} = \left(\frac{a_P}{r_{1,2}} \right)^2, \tag{37}$$

where $\mathrm{r}_{1,2}$ is the distance between planet and star, and $\mathrm{a_P}$ is the planet's semi-major axis. Furthermore, the mutual occultation of each star is considered as a rate by which the background star's light is blocked relative to its total radiation. That is,

$$\tau_{1,2} = \frac{A_{1,2} - A_{2,1}}{A_{1,2}}, \tag{38}$$

where the numerator on the right side describes the projected area of the background star which is not obscured, and the denominator is the total (cross-sectional) area of the background star. If the foreground star has at least the same diameter as the background star, τ of the background star drops to zero. The background star is determined by comparing the planet-star distances r_1 and r_2.

Finally, Eqs. (31), (32), (33), (36), and (37) are combined accordingly to get an equation for the short- and long-wavelength TOA insolation of the binary star

$$F_{TOA,sw}(\phi,\lambda) = E_{sw} \cdot \left[S_1 \cdot \rho_1^{-2} \cdot \tau_1 \cdot \theta_1(\phi,\lambda) + S_2 \cdot \rho_2^{-2} \cdot \tau_2 \cdot \theta_2(\phi,\lambda) \right], \tag{39}$$

$$F_{TOA,lw}(\phi,\lambda) = E_{lw} \cdot \left[S_1 \cdot \rho_1^{-2} \cdot \tau_1 \cdot \theta_1(\phi,\lambda) + S_2 \cdot \rho_2^{-2} \cdot \tau_2 \cdot \theta_2(\phi,\lambda) \right], \tag{40}$$

which are in accordance with Eqs. (5) and (6) for a single star. An example for the binary insolation is illustrated in Fig. 7 showing the total binary insolation and the individual contribution of the primary and secondary star. The rapid drops over a few time steps are caused by the mutual occultation of the stars. The secondary is smaller than the primary and thus causes only a partial occultation of the primary, while the secondary is fully eclipsed by the primary.

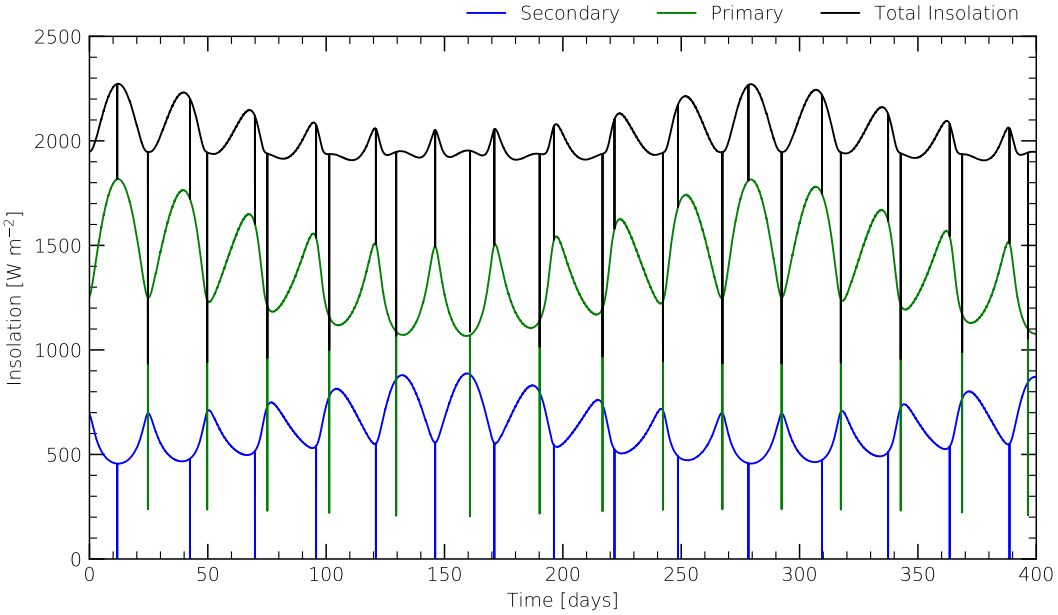

Figure 7: TOA insolation of the same test system as in Fig. 6. Insolation of the secondary is shown in blue, that of the primary in green. The total solar insolation of the binary is the sum of both and is shown in black. The brief drops in insolation are caused by the mutual occultation of the stars. The short-periodic variation ($\sim$25 days) is caused by the binary motion, the long-periodic variation of $\sim$270 days is caused by the eccentric orbits of the binary and the resulting variation of the planet-star distance. Note that the planetary eccentricity is zero.

2.4 Limitations of the modified PlaSim Code

The modified PlaSim code presented above has some important limitations that should be mentioned. First and foremost, this code is developed *only* for circumbinary planets and can not be applied to circumstellar systems, because the planetary orbit is in barycentric coordinates and thus with respect to the center of mass of the binary. The orbit of the secondary star would have to be transformed to heliocentric coordinates in order to simulate circumstellar systems. Moreover, there is no chemical model implemented in PlaSim so that the atmospheric composition can not be changed and is thus assumed to be Earth-like. Only the CO_2 concentration can be changed. The spectral partitioning is not only used for the computation of the TOA radiation, but also for cloud-radiation interactions making the implementation of different partitioning factors for each star challenging. Additional modifications

of the radiation transfer code would be required and thus limits the application to binary stars of the same spectral type. It should also be mentioned that the calculation of the binary isolation is not working properly when using the restart mode (where the final state of a previous simulation is used as an initial state), as the initial position of the planet is assumed to be in the perihelion, which is not guaranteed with the restart mode. Further restrictions and their implications are discussed in section 5.

3 Model Setup and Methodology

The modified PlaSim code introduced in section 2 is used to simulate the climate of circumbinary planets. In the first study (section 4.1) the Kepler-35 system is investigated and results are compared with those from Popp and Eggl (2017) (hereafter PE17). Kepler-35 is a G/G-binary system harboring one planet at ∼0.6 au with a mass of ∼0.13 M_J. Haghighipour and Kaltenegger (2013) find the habitable zone of Kepler-35 to be between 0.83 and 2.18 au. I follow the approach of PE17 and assume that the planet in Kepler-35 is a hypothetical Earth-like aqua-planet. At first, the climate state of the fictitious planet is examined for the same semi-major axes as examined by PE17, and globally as well as zonally averaged quantities are compared. The Kepler-35 HZ limits that are obtained with the modified PlaSim are then examined and also compared with the PE17 results. To infer the inner HZ limit, a specific humidity (as a good substitute for the mixing ratio) of 1 g kg^{-1} within the stratosphere (at 100 hPa height) is considered as threshold to the moist Greenhouse state. The sea ice extent and effective albedo is used to infer the outer HZ limit (transition to Snowball state). In a last step, the temporal variability of different climate indicators, such as surface temperature and total precipitation, are investigated and summarized. Orbital and stellar parameters are adopted from PE17 and are listed in table 1 and 2.

System	a_B [au]	e_B	a_P [au]	e_P
Kepler-35	0.1760	0.0000	0.90–1.30	0.0100
Kepler-1647	0.1276	0.1602	2.13–3.73	0.0581
Kepler-47	0.0836	0.0234	0.70–1.00	0.1000

Table 1: List of orbital parameters for the systems investigated in this work. Parameters for the Kepler-35 system are adopted from Popp and Eggl (2017). Kepler-1647 and Kepler-47 parameters are taken from Kostov et al. (2016) and Orosz et al. (2012). The semi-major axis is denoted as a and the eccentricity as e. Indices B and P refer to binary and planetary parameters, respectively.

The second study (section 4.2) investigates the climate and habitability of a planet in the Kepler-1647 binary system. Kepler-1647 harbors a F- and G-type star with masses $M = 1.22\ M_\odot$ and $M = 0.97\ M_\odot$, respectively. The circumbinary planet Kepler-1647b is a Jupiter-like gas giant with $M = 1.52\ M_J$ orbiting the system at 2.72 au, well within the HZ limits (Kostov et al. 2016). Even though Kepler-1647b can not be habitable, there is the possibility of habitable moons orbiting the planet. It is thus assumed that the planet under investigation is Earth-like and a natural satellite of Kepler-1647b. Effects such as tidal heating, planetary insolation and eclipses caused by Kepler-1647b are neglected. The HZ limits are, again, inferred from the atmospheric water vapor content and sea ice cover. Furthermore, the climate and habitability of a desert planet (no oceans or other larger water reservoirs) is investigated by performing additional simulations without the

aqua-planet mode. The inner HZ limit for the desert planet is determined using a threshold of 415 W m^{-2} net solar insolation, as found by Abe et al. (2011) for a planet orbiting a single star. The outer HZ limit is located where the zonally averaged surface temperature at the equator is below the freezing point. Orbital and stellar parameters are taken from Kostov et al. (2016) and summarized table 1 and 2.

In the last study the Kepler-47 circumbinary system is investigated. Kepler-47 is the first multi-planet system that has been discovered by the Kepler mission harboring three Neptune-like planets with masses between 8 and 23 $M_\oplus$. The three planets are orbiting the G6V/M4V binary star at ∼0.3, 0.7 and 1.0 au, with the outer planet being well within the habitable zone limits (0.99 and 1.75 au) found by Pilat-Lohinger et al. (2019). Here again, it is assumed that the planet under investigation is an Earth-like moon, and the climate and HZ limits are investigated using zonal averages and vertical profiles. Parameters are taken from Orosz et al. (2012) and listed in table 1 and 2.

System	M_1 [$M_\odot$]	R_1 [$R_\odot$]	T_1 [K]	M_2 [$M_\odot$]	R_2 [$R_\odot$]	T_2 [K]
Kepler-35	0.8870	1.0284	5606	0.8094	0.7861	5202
Kepler-1647	1.2200	1.7900	6210	0.9700	0.9660	5770
Kepler-47	1.0430	0.9640	5636	0.3620	0.3506	3357

Table 2: List of stellar parameters. For references see table 1. Here, M is the mass, R is the radius, and T is the surface temperature of the star. Index 1 and 2 refer to the host and companion star, respectively.

Table 3 lists all PlaSim parameters that are relevant for this thesis. These parameter values are used in all subsequent studies, unless otherwise specified. The surface albedo for open water is hard-coded in PlaSim and is by default set to 0.069. The sea-ice albedo is a function of the ice surface temperature and has a maximum value of 0.7. The cloud albedo depends on the cloud level and is defined for the visible and IR band (see table 3.1 in PlaSim's reference manual). Predefined albedo values are not changed, but important for interpreting results. Furthermore, the aqua-planet mode and the calender day of vernal equinox are by default 0 and 80.5, respectively, and are set to 1 and 0 for these studies. The default spectral partitioning values are valid for a G-type main-sequence star and are also not changed. Thus, it is assumed that the three systems under investigation are G/G-binaries.

Other parameters are read from *namelist* files and are mostly self-explaining. However, at this point it is important to mention that the number of days per year is computed with the third law of Kepler. If the computed length of a year is longer than the default length of 365 days, the number of days per month has to be extended such that 12 months cover the number of days per year. The parameter *N_DAYS_PER_MONTH* is not defined in the namelist, if the length of a year is ≤365 days. The solar constant, which is read from the file *planet_namelist*, is used

only for single star simulations. All simulations are performed with 10 vertical levels and T21 spectral resolution, which is equivalent to 32×64 grid points, or 5.6 degree horizontal resolution.

Parameter	Value	Comment	
NLEV	10	Number of atmospheric levels, in plasimmod.f90	hard-coded
zsolar1	0.517	Spectral partitioning visible fraction, in radmod.f90	
zsolar2	0.483	Spectral partitioning IR fraction, in radmod.f90	
ve	0.	Calender day of vernal equinox, in radmod.f90	
albsea	0.069	Albedo for open water, in seamod.f90	
albice	$\leq$0.7	Max. albedo for sea ice, seamod.f90	
naqua	1	Switch to aqua planet mode	plasim_nl
NOUTPUT	1	Enables output file	
MPSTEP	45	Length of a time step in minutes	
N_RUN_YEARS	80	Number of years to run	
N_DAYS_PER_YEAR	*	Number of days per year	
N_DAYS_PER_MONTH	*	Number of days per month	
NFIXORB	1	Use predefined planetary orbits	planet_nl
OBLIQ	0.	Obliquity for fixed orbits in degree	
MVELP	0.	Longitude of vernal equinox for fixed orbits in degree	
GSOL0	*	Solar constant in W m^{-2}, only used in single star simulations	
sel_bin	1	Enables binary star mode	binary_nl
sel_StefanBoltzmann	1	Use Stefan Boltzmann law to compute stellar luminosities	
dt	225.	Time step of one binary integration step in seconds	
NOCEAN	1	Enables ocean model, defined in oceanmod_nl	
NICE	1	Enables sea ice model, defined in icemod_nl	

Table 3: List of parameters that are relevant for this thesis. Parameters in the upper section are hard-coded within the PlaSim code, while all the other parameters are read from different input files. Note that the number of atmospheric levels can be changed in the graphical user interface (called *model starter*) of PlaSim. The asterisk refers to variable parameter values. See text for further explanation.

4 Results

4.1 Kepler-35

This section presents results of an aqua-planet in the Kepler-35 system. Figure 8 shows the zonally averaged surface temperature T_S, total precipitation, total cloud cover, and effective albedo of four models using the same semi-major axes (1.14, 1.165, 1.195, and 1.225 au) as in PE17. All lines are temporal averages over 10 Earth-years in steady state. The effective albedo is computed as the ratio of reflected and incoming irradiation at the TOA. The dotted black line in the T_S panel illustrates the freezing point of water at 273.15 K. A comparison with the PE17 results (see Fig. 3) reveals that the differences among individual models are smaller when using PlaSim, especially for semi-major axes between 1.14 and 1.195 au, where the zonal structure of the shown quantities is very similar. The surface temperature and effective albedo indicate glaciation up to 30°–60° latitude (with clearly positive temperatures near the equator) for the models between 1.14 au and 1.195 au implying that the planet is not in the Snowball state at any of these distances. As in the PE17 finding, planets beyond 1.225 au transition into a Snowball state in which the temperature is clearly negative at all latitudes, with no significant precipitation. Furthermore, in none of these four models does the specific humidity in the stratosphere (not shown) exceed the threshold of 0.1 % (or 1 g/kg; transition to the moist Greenhouse state). Thus, a planet with a semi-major axis of between 1.14 and 1.195 au is habitable when PlaSim is used, and only the aforementioned models are considered. Globally averaged quantities in steady state are summarized in table 6.

Model	TSI [W m^{-2}]	T_S [K]	Precip. [mm day^{-1}]	Sea ice cover	Albedo
1.140 au	1390.54	290.92	4.17	0.18	0.33
1.165 au	1330.94	277.76	2.99	0.30	0.37
1.195 au	1265.43	261.09	1.89	0.45	0.44
1.225 au	1204.66	206.23	0.00	1.00	0.67

Table 4: Global averages over 10 Earth-years of the total solar insolation TSI, surface temperature T_S, precipitation P, sea ice cover, and effective albedo for semi-major axes used in PE17.

Figure 9 shows the same as Fig. 8, but for planetary semi-major axes where globally averaged surface temperatures (temporal mean over 10 Earth-years) coincide with those of PE17, which is at 0.95, 1.14, 1.18, and 1.32 au. Despite different semi-major axes, the resulting climate states are similar to those from PE17. In the hottest model, at 0.95 au, the planet is clearly in the moist Greenhouse state, with a specific humidity of >20 g kg^{-1} in all atmospheric levels (not shown). The zonal mean of the effective albedo and sea-ice extent (also not shown) indicate that

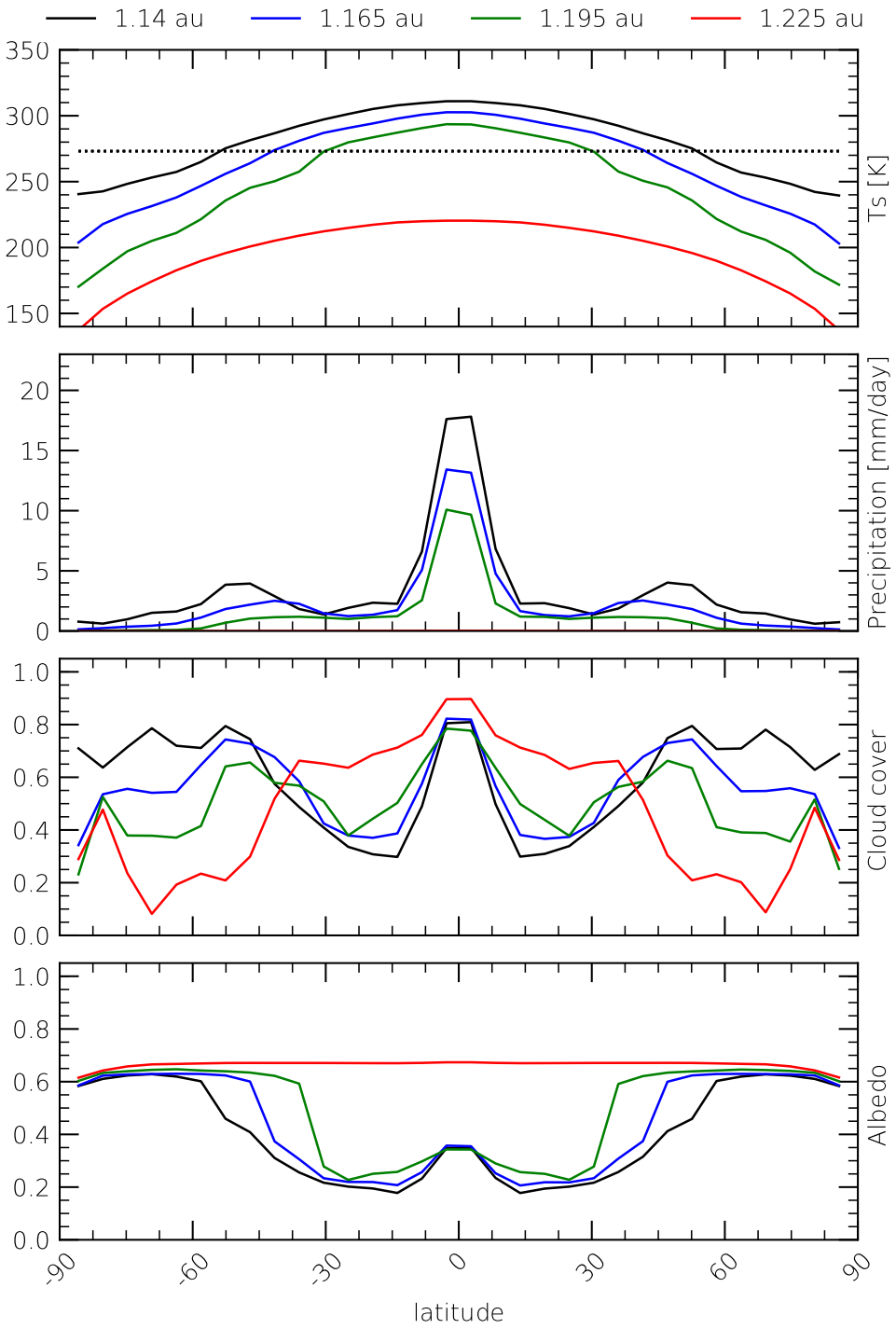

Figure 8: Zonal averages of the surface temperature, precipitation, total cloud cover, and effective albedo for a planet with a semi-major axis of 1.14 au in black, 1.165 au in blue, 1.195 au in green, and 1.225 au in red. Each line represents an temporal average over 10 Earth-years in steady state. Note that these are the same semi-major axes as used by PE17, and thus comparable with Fig. 3. The black dotted line in the upper panel denotes the freezing point at 273.15 K.

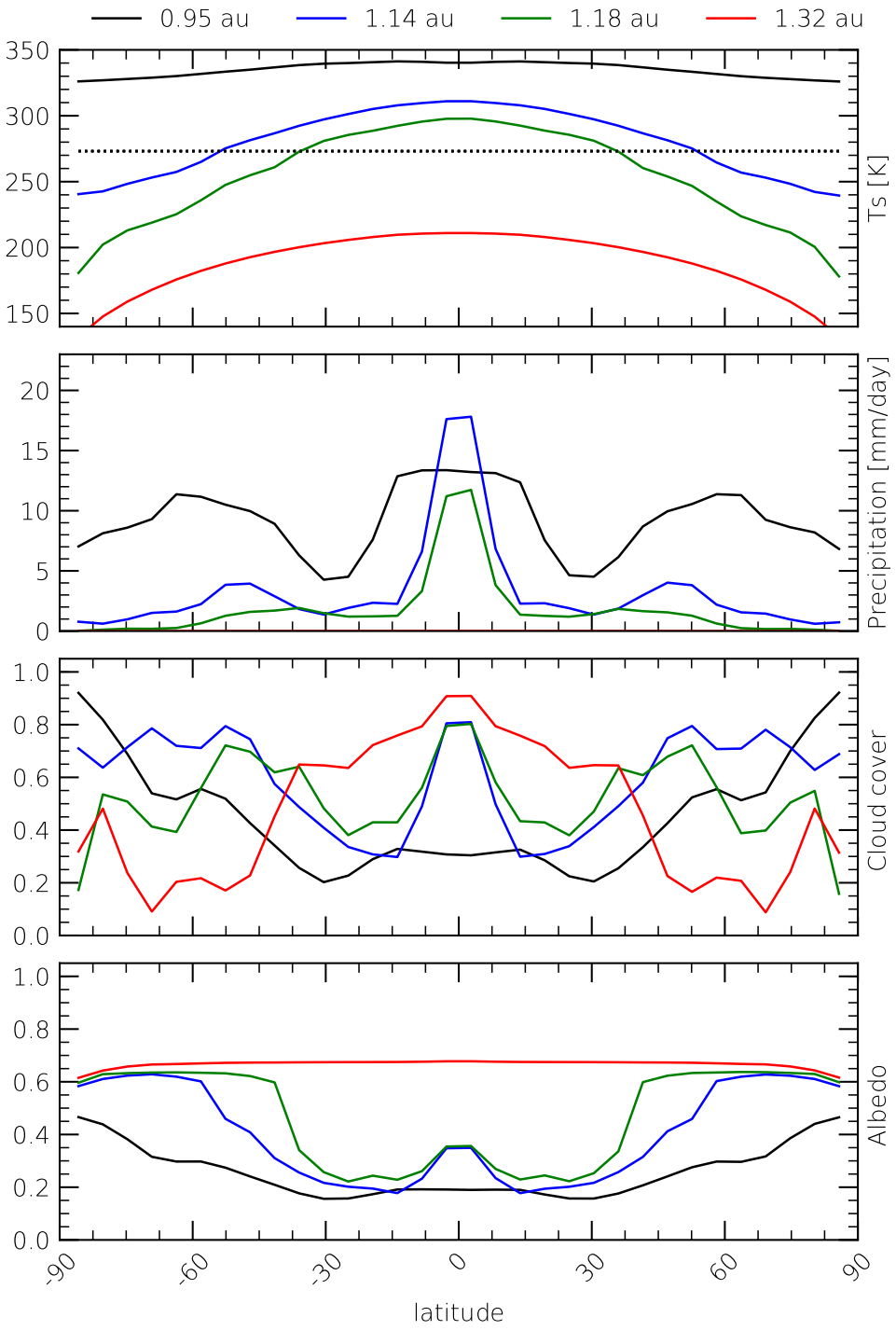

Figure 9: As in Fig. 8, but for semi-major axes where the globally averaged surface temperature matches that of PE17. Here, planetary semi-major axes ranges from 0.95 to 1.32 au. Note that a planet with a semi-major axis of 0.95 au is in the moist Greenhouse state, whereas at 1.32 au the planet is in Snowball state. For a semi-major axis of between 1.14 and 1.18 au, the planet is in habitable state, with glaciation only near the poles.

there is no sea-ice in this model. The large effective albedo at high latitudes stems from the large amount of clouds in this region. This model is qualitatively similar to the PE17 result for a planet with a semi-major axis of 1.14 au. Moreover, the intermediate models at 1.14 and 1.18 au in Fig. 9 are qualitatively similar to the PE17 results at 1.165 and 1.195 au. Both models exhibit positive temperatures near the equator and glaciation of the poles. Furthermore, in both models is the specific humidity (not shown) in the stratosphere well below the threshold for the transition into moist Greenhouse state, which indicates that a planet with a semi-major axis of between 1.14 and 1.18 au is in habitable state. The total precipitation and cloud cover peak at the equator, slightly decrease between 10°–30° latitude, and peak again at high latitudes. Note that this meridional structure is similar to the mean climate state of the Earth, as it is expected from an Earth-like model. The coldest model in Fig. 9 (1.32 au) is in Snowball state (full glaciation) and exhibits no precipitation, which agrees well with the PE17 result for a semi-major axis of 1.225 au. While zonal averages of T_S, P, and effective albedo are similar to those from PE17, the total cloud cover is remarkably different at all latitudes. It has a peak near the equator, with values up to 0.9, and decreases towards the poles, whereas PE17 has no clouds at all in the Snowball state. I presume that the different cloud parameterization schemes of the two models could be a possible explanation for this.

To infer the inner HZ limit of Kepler-35 using the modified PlaSim code, vertical profiles of the specific humidity (SH) are examined, which are presented in Figure 10. It shows globally averaged SH profiles for a planet with a semi-major axis of 1.12 and 1.14 au. It also shows profiles for 1.12 au that are zonally averaged over the equator and polar region, respectively. At 1.14 au, the specific humidity has a maximum of $\sim$15 g kg^{-1} at the surface, which slowly decreases with height. It drops to the threshold value of 1 g kg^{-1} at 200 hPa and further decreases to $\sim$0.2 g kg^{-1} at 100 hPa height (lower stratosphere). Consequently, a planet with a semi-major axis of 1.14 au is in habitable state (no global glaciation as shown in Fig. 9). At 1.12 au, SH has a globally averaged maximum of 30 g kg^{-1} near the surface and decreases to $\sim$3 g kg^{-1} at 100 hPa height. The zonally averaged profiles reveal that the SH is even higher at the equator, with a maximum of $\sim$55 g kg^{-1} near the surface and a minimum of 8 g kg^{-1} in the stratosphere. In the polar regions, it already drops to 1 g kg^{-1} at 400 hPa height. Thus, hydrogen escape mainly takes place in low latitudes, and the transition to the moist Greenhouse state occurs between 1.12 and 1.14 au.

Figure 10 also shows vertical profiles of the relative humidity RH and air temperature T, which are arranged in the same way as profiles of SH. Almost all RH profiles decrease rapidly within the boundary layer (1000–800 hPa) and remain relatively constant between 800 and 200 hPa height. Above 200 hPa, the differences between habitable state and moist Greenhouse state are visible. In the former case, RH decreases in the stratosphere, while it shows a weak increase in the moist Greenhouse state. Note that these profiles are spatial and temporal averages so that cloud formation is also possible for RH $<$ 100 %. The shape of the globally averaged temperature profile is very similar in both states. In the moist Greenhouse state,

globally averaged air temperature has a maximum of ∼305 K near the surface and reaches the freezing point at 350 hPa height. In habitable state, temperatures are in general ∼15 K lower and the freezing point is reached at 600 hPa height. The temperature profiles of the equator and polar region need no further explanation.

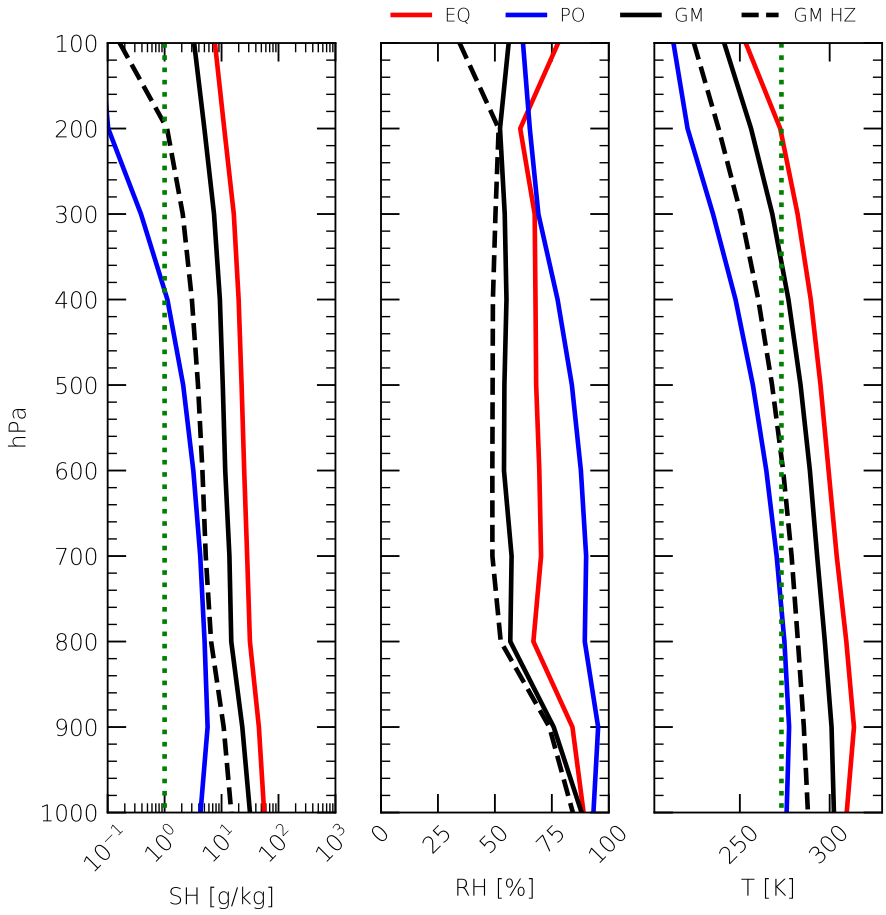

Figure 10: Vertical profiles of the specific humidity SH, relative humidity RH, and air temperature T between 1000 and 100 hPa. Black lines illustrate globally averaged profiles, and the blue and red lines indicate zonal averages over one latitude at the north pole and equator, respectively. Solid lines refer to a planet in the moist Greenhouse state (1.12 au), dashed lines to a planet in habitable state (1.14 au). The green dotted line in the SH panel illustrates the threshold of 1 g kg^{-1} and that in the temperature panel denotes the freezing point at 273.15 K. All lines are temporal averages over 10 Earth-years in steady state.

The outer HZ limit is determined based on the zonally averaged albedo and sea-ice cover (not shown). Figure 11 shows the same as Fig. 8, but for planetary semi-major axes of 1.12, 1.14, 1.21, and 1.22 au. The effective albedo reveals that the transition to the Snowball state occurs between 1.21 and 1.22 au. At a semi-major axis of 1.21 au, the planet has relatively large areas (±30 degree) of open water around the equator where no sea ice is formed. At 1.22 au, the planet goes into a Snowball

state, with negative temperatures and nearly constant albedo at all latitudes. Note that the effective albedo of ∼0.7 is equivalent to the prescribed sea-ice albedo (see section 3). The zonally averaged cloud cover has, again, a very prominent structure, as seen for a semi-major axis of 1.30 au (see Fig. 9). It exhibits the highest value of ∼0.9 among the four models near the equator, which drops to the smallest value of ∼0.1 at higher latitudes. Again, this is in contradiction to the PE17 results for a planet in Snowball state, and shows that the results can strongly vary between different climate models.

Figure 12 illustrates various time series for the four models presented in Fig. 11. It shows the globally-averaged total solar irradiation TSI, surface temperature T_S, total precipitation, sea-ice cover, and effective albedo over a period of five Earth-years in steady state. The changes in the TSI consist of two periods, a short-periodic signal of ∼22 days, which is caused by the motion of the binary star around its barycenter, and a long-periodic signal caused by the eccentric orbit of the planet, which has a period of 332, 341, 365, and 387 days for the given semi-major axes. The temporal variability of the sea-ice cover and effective albedo is in all four models very small indicating they are barely affected by the strong TSI fluctuations. Moreover, we can see that the variability of the surface temperature increases with increasing semi-major axis, while that of precipitation and effective albedo is largest in the innermost model at 1.12 au.

Model	Single Star		Binary Star	
	Amplitude [K]	Variance [K]	Amplitude [K]	Variance [K]
1.12 au	0.13	0.004	0.13	0.004
1.14 au	1.10	0.123	1.11	0.132
1.21 au	1.75	0.313	1.83	0.457
1.22 au	1.07	0.401	2.00	0.844

Table 5: Amplitude and variance of surface temperature anomaly in the models presented in Fig. 11 for both single star and binary star simulations. The binary insolation clearly increases the variability of the surface temperature.

The temperature time series from Fig. 12 are again highlighted in Fig. 13, but are averaged to zero (i.e., subtracting the 10 Earth-year average). The figure shows that the variation is indeed largest (amplitude A = ∼2.0 K) for the outermost orbit at 1.22 au. It clearly exhibits the short- and long-periodic signal of the binary insolation, and has a fairly large correlation $\rho = 0.8$ with it. In the moist Greenhouse state, only the long-periodic signal of the insolation is present, with A = ∼0.1 K and $\rho = 0.0$. In the habitable state, at 1.14 and 1.21 au, the temperature variation has a rather chaotic behavior and shows no clear dependency on the TSI. At 1.14 au, the temperature varies with an amplitude A = ∼1.1 K and has a relatively small correlation $\rho = 0.1$ with the TSI. At 1.21 au, the temperature variation has a larger amplitude A = 1.8 K and correlation $\rho = 0.5$, but is in general smaller than that

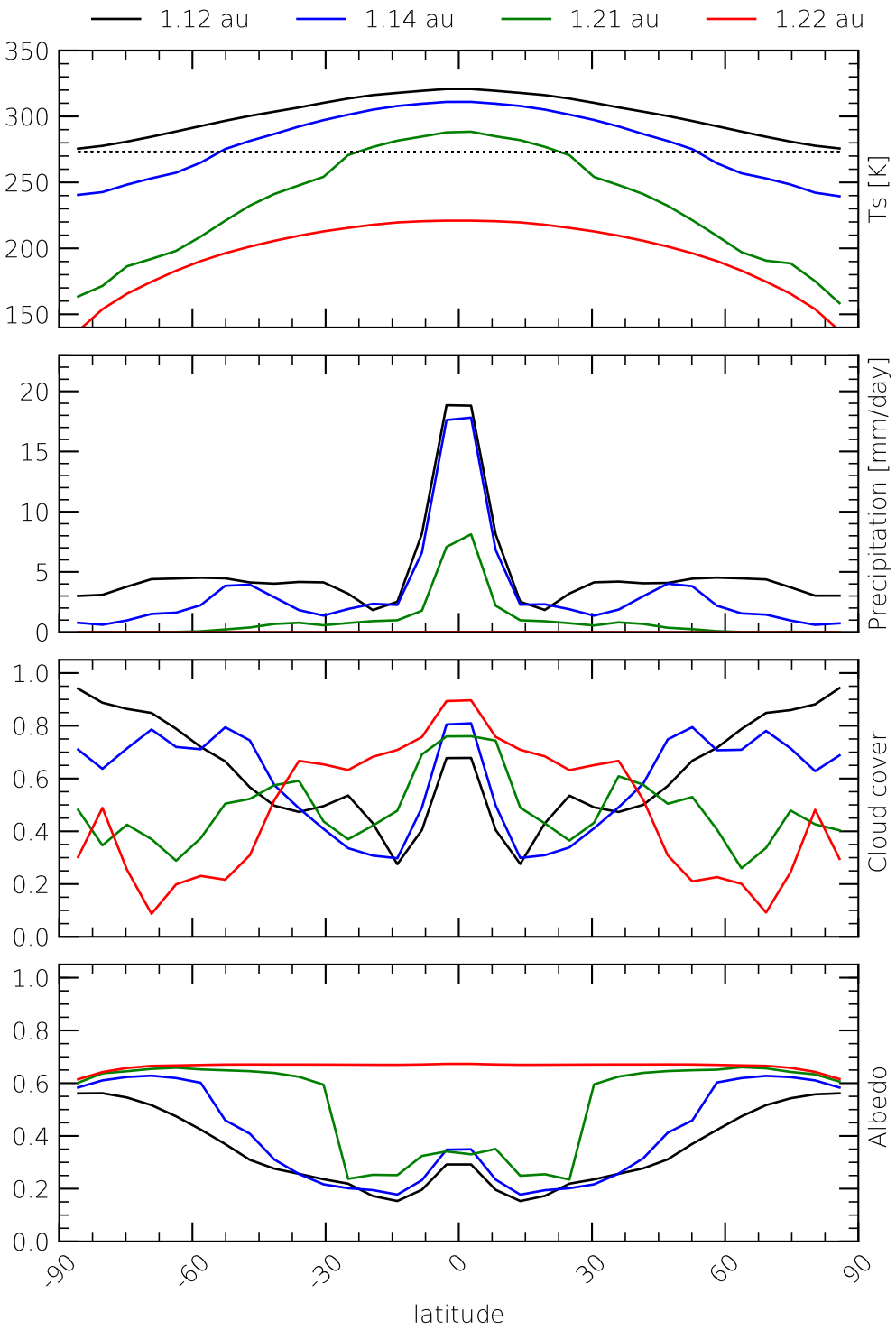

Figure 11: As in Fig. 8, but for a planet with a semi-major axis of 1.12 au (black lines), 1.14 au (blue), 1.21 au (green), and 1.22 au (red). At 1.12 au, the planet is in the moist Greenhouse state as shown in Fig. 10. At 1.22 au, the planet is in Snowball state. Note that there is no precipitation in this state. A planet with a semi-major axis of between 1.14 au and 1.21 au is in habitable state.

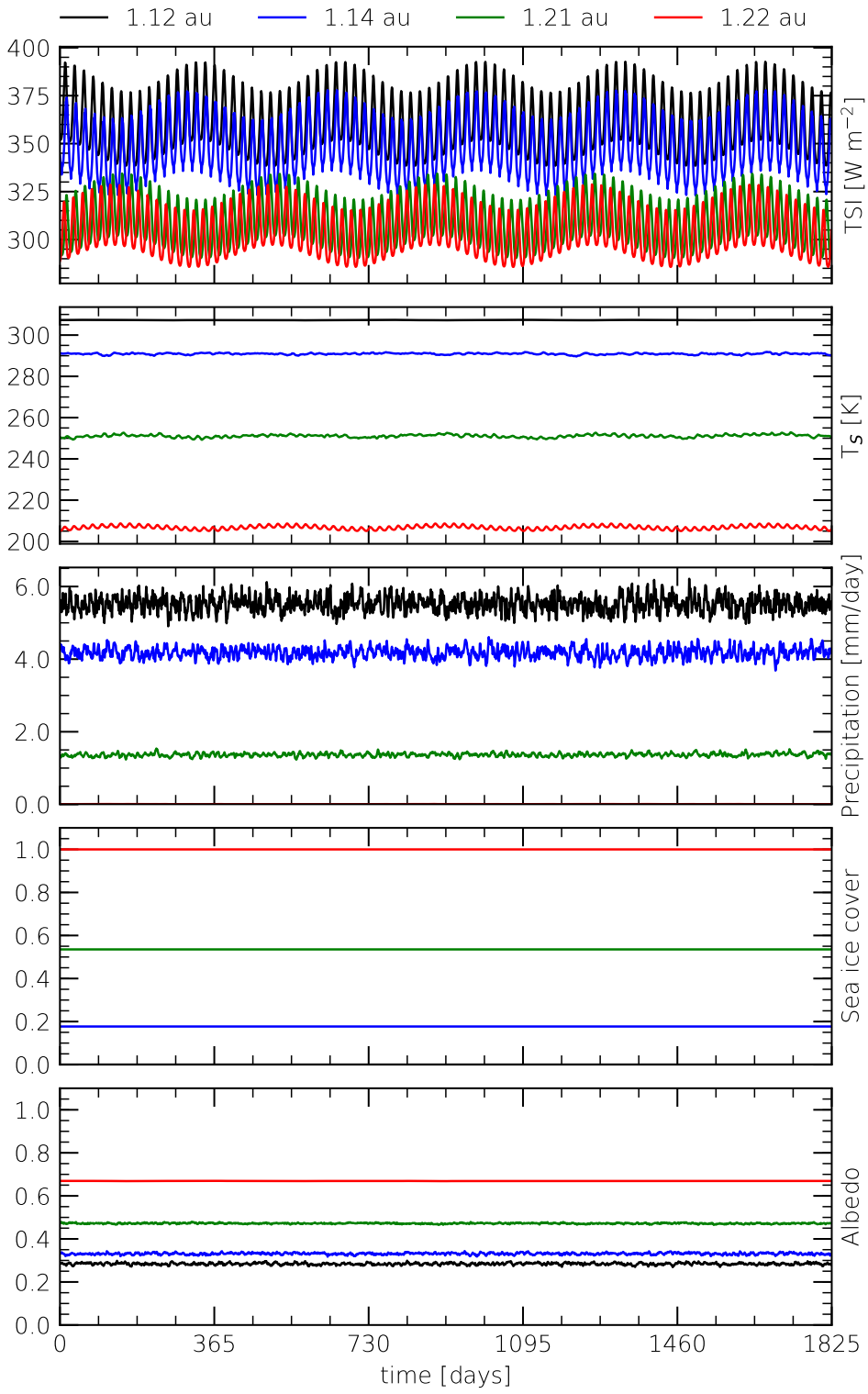

Figure 12: Time series plot over five Earth-years in steady state. It shows global averages of the total solar insolation TSI, surface temperature T_S, precipitation, sea ice cover, and effective albedo of the four models presented in Fig. 11 (with the same color coding).

of a planet in Snowball state. Corresponding variances are listed in table 5. This may be interpreted as follows. Processes that can affect the surface temperature are somewhat suppressed in the Snowball state leading to a temperature variation merely caused by the variation of the binary insolation. That is, there is no precipitation that can cool the planet's surface, and there is little or even no variation in the effective albedo that may effect the amount of absorbed irradiation. In the habitable state, precipitation and effective albedo exhibit moderate variability so that the temperature is not only affected by the variation of the TSI. In the Greenhouse state, the surface temperature seems relatively insensitive to rapid changes in both insolation and total precipitation. Therefore, only the long-periodic signal of the TSI can be seen in the surface temperature.

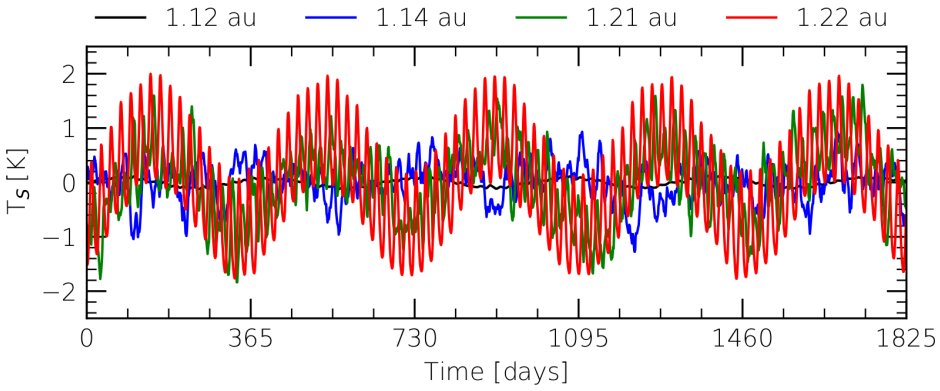

Figure 13: Time series of the globally averaged surface temperature as presented in Fig. 11, but averaged to zero by subtracting its 5-years mean.

To emphasize the interpretation above, additional reference simulations of a single star system are performed. The single star insolation is set to the arithmetic mean of the total binary insolation during the first few time steps. The corresponding temperature time series over five Earth-years in steady state are illustrated in Fig. 14. It shows a similar behavior as seen in the binary setup. In Snowball state, the vari-

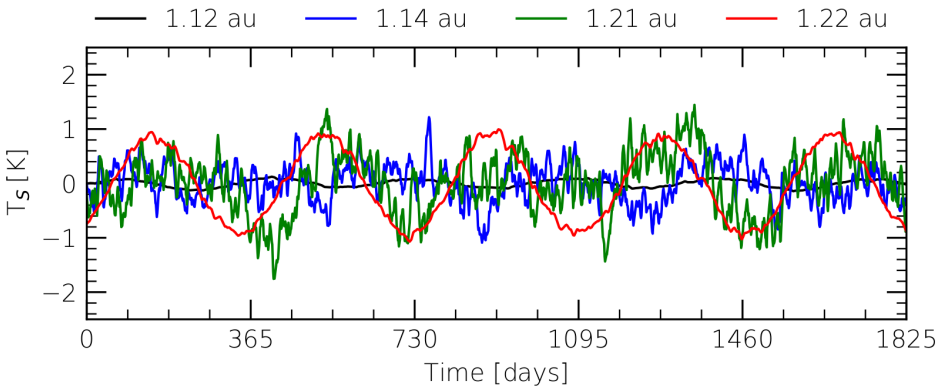

Figure 14: As in Fig. 13, but for single star insolation.

ation of the planet's surface temperature merely follows the signal of the single star insolation (not shown), i.e. without a short-periodic signal and thus with a smaller amplitude A = 1.1 K and variance σ^2 = 0.4 K. For a planet with a semi-major axis of 1.12 au, the variation is very similar to that of its binary analogue, with A = 0.1 K and σ^2 = 0.004 K. In the habitable state, the temperature variation is also reduced compared to that of its binary analogue (A = 1.10 K and σ^2 = 0.12 K for 1.14 au, and A = 1.75 K and σ^2 = ∼0.31 K for 1.21 au), but not as strong as in the Snowball state. This finding shows that the temperature variability in non-habitable states is solely driven by the variation of the TSI, and is more chaotic in the habitable state, which underlines the interpretation above. Furthermore, we have seen that the binary insolation increases the variability of the surface temperature, especially in states where the surface temperature is solely affected by the signal of the insolation. That is, the stronger the TSI signal is present in the surface temperature, the stronger is the increase in its variation. Amplitude and variance values of the surface temperature of the single star simulations are also summarized in table 5.

To finalize this study, vertical profiles of SH, RH, and air temperature of the outermost model (1.22 au) are illustrated in Fig. 15. The specific humidity is below

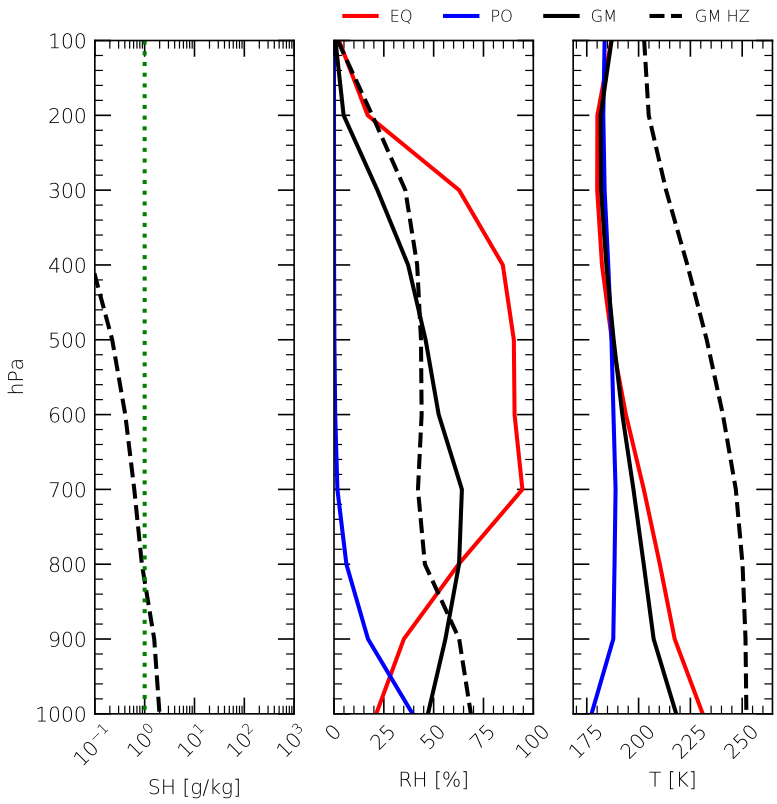

Figure 15: As in Fig. 10, but for an aqua-planet in Snowball state at 1.22 au (solid lines). The dashed lines denote a planet within the habitable zone, with a semi-major axis of 1.21 au. Note that all T-profiles are below the freezing point, and SH of the planet in Snowball state is well below 0.1 g kg^{-1} at all latitudes and heights.

0.1 g kg^{-1} at all latitudes and heights. The air temperature is at all heights well below the freezing point such that only cold clouds can be formed. The relative humidity emphasizes the zonal profile of the total cloud cover (see Fig. 11). The middle troposphere in the equator region exhibits a RH of up to ∼95 % reflecting the large cloud cover in that region, while it steadily decreases towards the poles. Table 6 summarizes the four models presented in Fig. 11.

Model	Period [days]	TSI [W m^{-2}]	T_S [K]	Precip. [mm/day]	Sea ice cover	Albedo
1.12 au	332	1442.66	307.30	5.52	0.00	0.28
1.14 au	341	1390.54	290.92	4.17	0.18	0.33
1.21 au	373	1235.26	251.11	1.37	0.54	0.47
1.22 au	378	1215.33	206.77	0.00	1.00	0.67

Table 6: List of orbital periods, total solar insolation as well as globally averaged precipitation, sea ice cover, and effective albedo of the Kepler-35 models presented in Fig. 11.

In summary, using PlaSim to simulate the climate of Kepler-35 leads to a slightly broader habitable zone compared to that found by Popp and Eggl (2017). A planet with a semi-major axis of between 1.14 and 1.21 au is still habitable when PlaSim is used. Furthermore, we have seen that the insolation of the binary increases the temporal variability of the planet's surface temperature.

4.2 Kepler-1647

In this section, results of the Kepler-1647 study are presented. As for the planet in the Kepler-35 system, climate states are derived from zonal averages and vertical profiles, which are presented in Fig. 16 and 17. For that, an aqua-planet with a semi-major axis of 2.12, 2.14, 2.24, and 2.25 au is investigated. The planet is habitable with a semi-major axis of between 2.14 and 2.24 au and goes into the Snowball state at 2.25 au, whereas a semi-major axis of 2.12 au leads to a moist Greenhouse state (see Fig. 17). Table 7 gives an overview of the four aqua-planet models in the Kepler-1647 system.

Figure 16 shows that the maximum in total precipitation is again at the equator, whereas there is no precipitation in the Snowball state at all. As in the Kepler-35 study, there are two peaks in the cloud cover of each model, except for the planet in Snowball state. One peak is at the equator, with values between 0.7 and 0.9, and another maximum is at higher latitudes, also with values up to 0.9, while it drops to ∼0.3 between the two maxima. The cloud cover in Snowball state is very similar to that in the Kepler-35 study, and thus not an individual case. The effective albedo (Fig. 16) and the vertical profiles of SH, RH, and air temperature (Fig. 17)

are also remarkably similar to what we have seen in the Kepler-35 study, and thus need no further discussion. Overall, it can be said that mean climate states in the Kepler-1647 system are very similar to those of a planet in Kepler-35, but for different semi-major axes.

Model	Period [days]	TSI [W m^{-2}]	T_S [K]	Precip. [mm/day]	Sea ice cover	Albedo
2.12 au	762	1408.80	303.77	5.23	0.02	0.29
2.14 au	773	1380.69	291.60	4.26	0.18	0.33
2.24 au	827	1257.97	261.57	1.94	0.45	0.43
2.25 au	833	1247.15	208.51	0.01	1.00	0.67

Table 7: As in table 6, but for the aqua-planet models in the Kepler-1647 system.

What is significantly different to Kepler-35 is the temporal variability of the quantities shown in Fig. 18. The long-periodic signal of the insolation exists in almost all quantities (except for the sea ice cover) of the four models. At this point, the temporal variability of precipitation and effective albedo in the habitable state (2.14 and 2.24 au) should be emphasized. Both quantities exhibit the long-periodic signal of the TSI, which is not the case in Kepler-35. Furthermore, it is evident that the surface temperature of all four models exhibits the long-periodic signal of the TSI, but not the short-periodic signal, as we have seen it in the outermost model of the Kepler-35 study. For comparison, the amplitude of the globally averaged surface temperature is 1.40 K, 2.27 K, 4.65 K, and 7.54 K for 2.12 to 2.25 au. Hence, the temporal variability of the surface temperature, precipitation, and effective albedo is considerably larger on a planet in the Kepler-1647 system, which can be attributed to the large TSI variation of $\sim$100 W m^{-2}. This is roughly twice as large as in Kepler-35.

Figures 16 and 18 also show results for a desert planet simulation with a planetary semi-major axis of 2.14 au, which is identical to the inner HZ limit of the aqua-planet. It becomes apparent that the desert planet has a significantly lower surface temperature compared to the aqua-planet, with largest differences ($\sim$90 K) on the poles. The globally averaged surface temperature exhibits the long-periodic signal of the TSI (amplitude $\sim$8 K) and is, on average, 25 K smaller than that of an aqua-planet with identical semi-major axis, because heat is barely stored in the dry soil masses. Furthermore, clouds and precipitation can exist only in the polar regions of the desert planet. Precipitation is on the order of $\sim$1.0 mm month^{-1} leading to an accumulated snow cover of roughly one meter after 80 years, which explains the increased albedo at high latitudes. The temporal evolution of the effective albedo of the desert planet shows no variation due to the lack of varying sea ice and cloud cover.

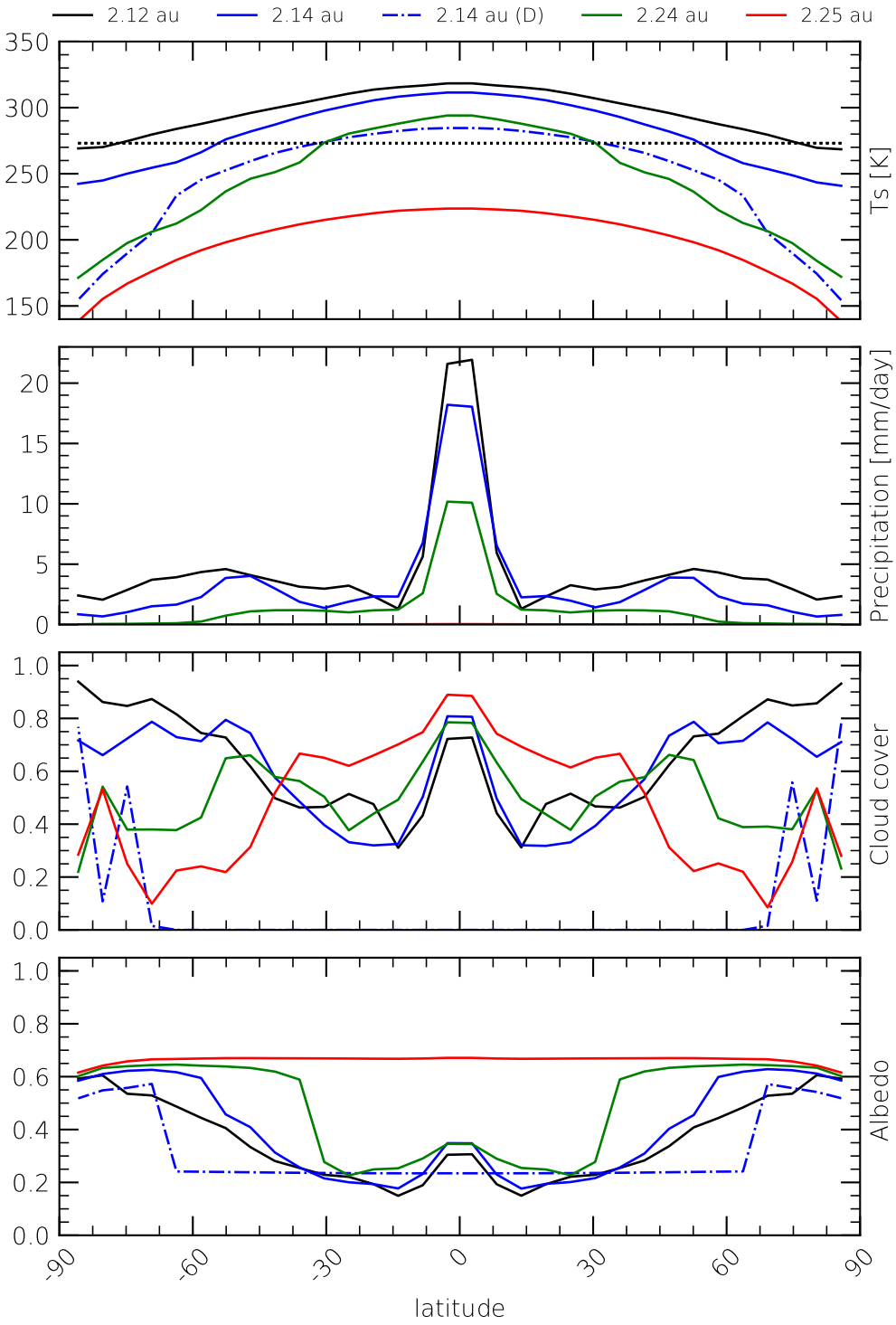

Figure 16: As in Fig. 11, but for an aqua-planet in Kepler-1647 with a semi-major axis of 2.12 au in black, 2.14 au in blue, 2.24 au in green, and 2.25 au in red. The solid lines refer to the aqua-planet models and the dash-dotted line to the desert planet model. Each line represents an average over 10 Earth-years in steady state.

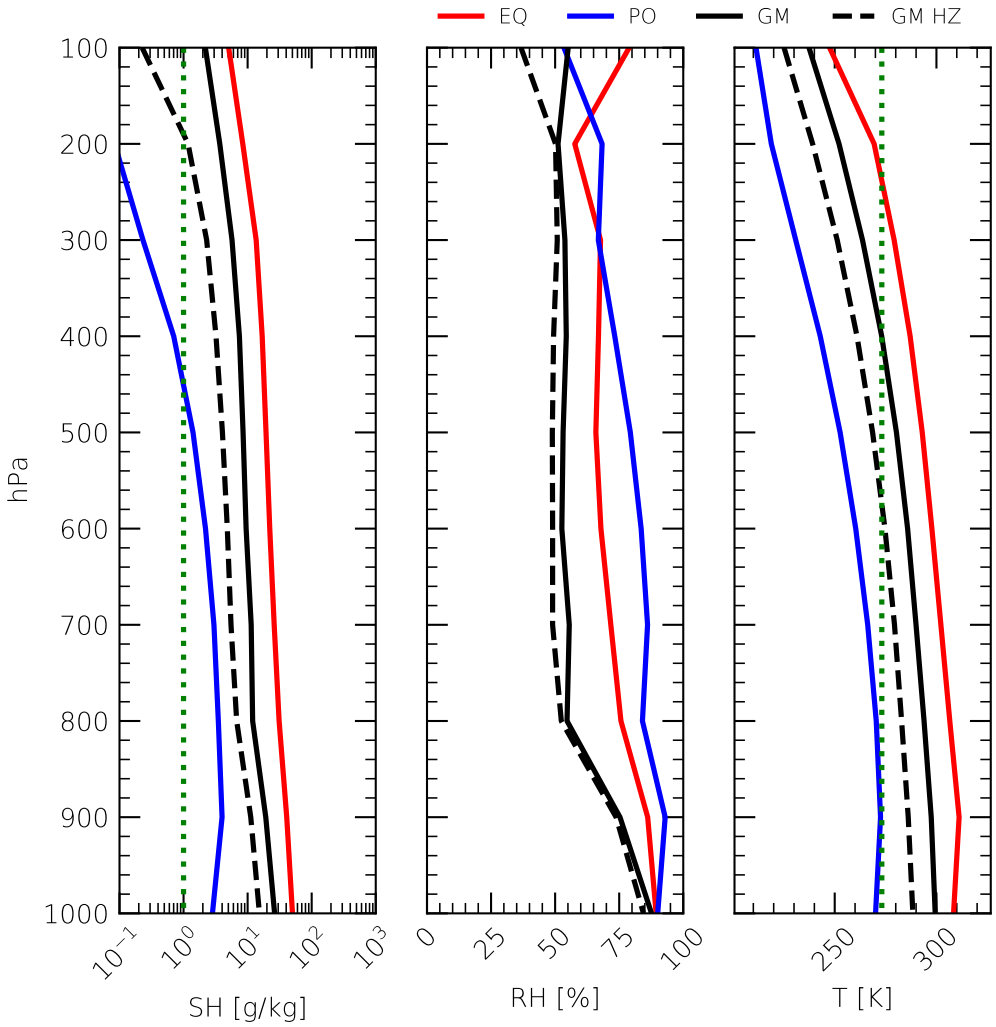

Figure 17: As in Fig. 10, but for an aqua-planet in the Kepler-1647 system with a semi-major axis of 2.12 au (solid lines; moist Greenhouse state). The dashed lines indicate global averages of a planet with a semi-major axis of 2.14 au, which is within the habitable zone of Kepler-1647.

In the following, HZ limits for a desert planet in the Kepler-1647 system are derived using Fig. 19, 20 and 21. It shows that the desert planet is habitable for a semi-major axis of between 1.90 and 2.30 au. At 1.80 au, the net solar insolation exceeds the threshold of 415 W m^{-2} during perihelion passages, with the possible consequence that surface water reservoirs start to evaporate. This is the transition to an uninhabitable state equivalent to the moist Greenhouse state of an aqua planet. At 1.70 au, the 10-years average of the net solar insolation exceeds the aforementioned threshold (not shown). If we go even closer to the star, numerical instabilities arise and the simulation terminates. On a planet with a semi-major axis of 2.35 au, the surface temperature is at all latitudes below the freezing point such that small reservoirs of surface water as well as soil moisture would freeze, which indicates the transition to a Snowball state. These figures also show that the climate states of the

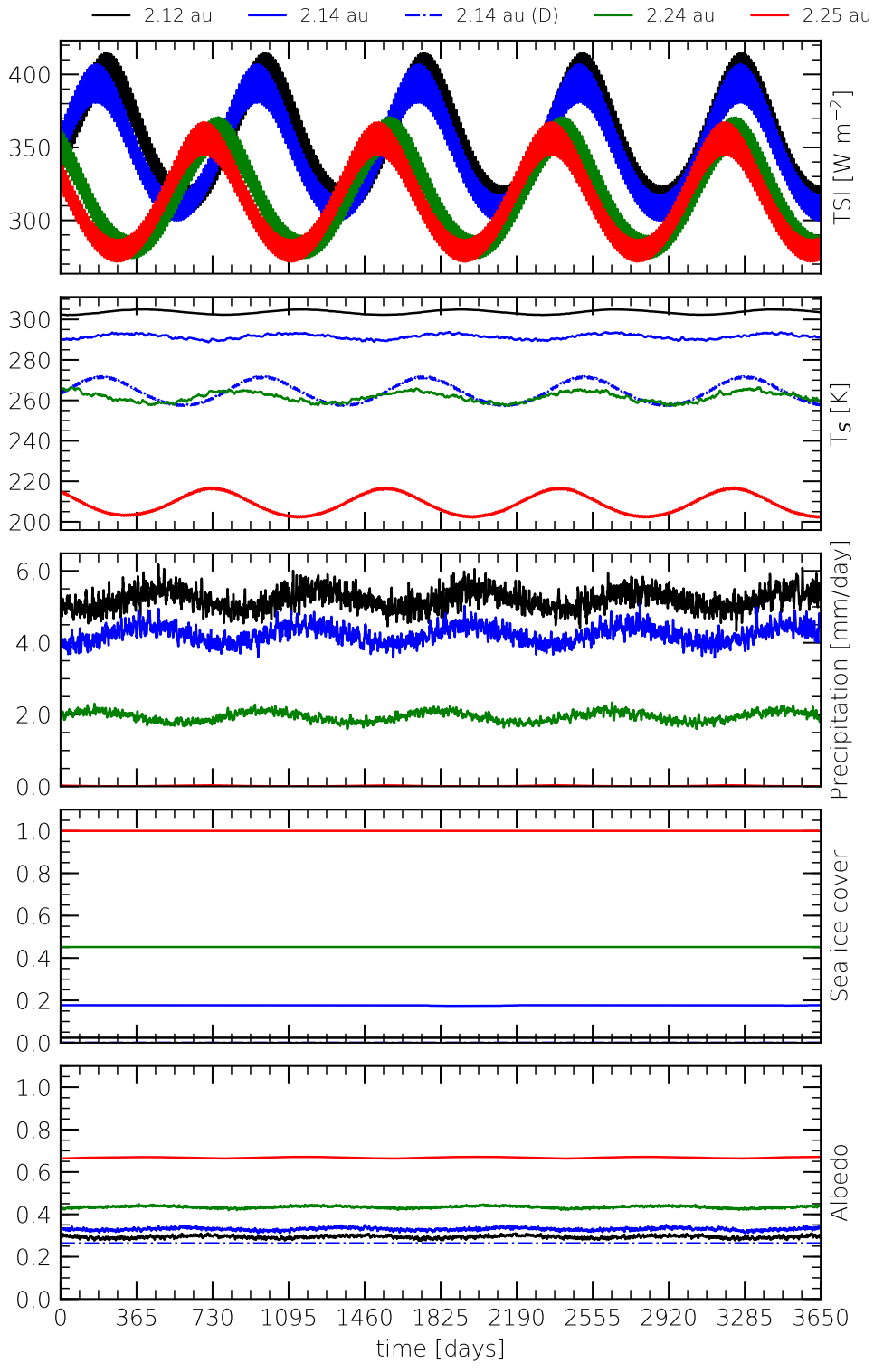

Figure 18: As in Fig. 12, but for an aqua-planet in the Kepler-1647 system with a semi-major axis of 2.12 au (black solid lines), 2.14 au (blue), 2.24 au (green), and 2.25 au (red). In addition, a desert planet model with a semi-major axis of 2.14 au is shown (blue dash-dotted lines).

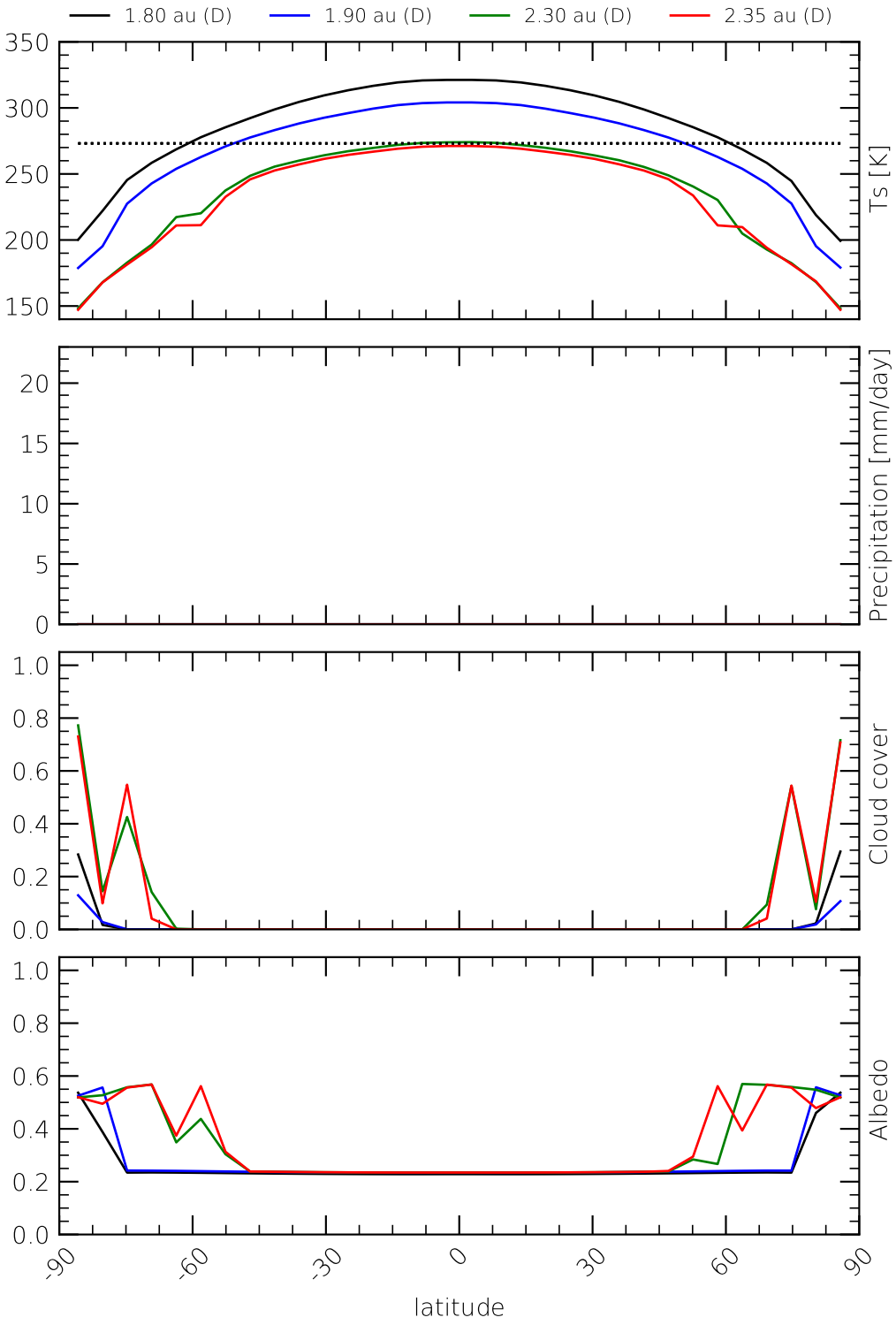

Figure 19: As in Fig. 16, but for the Kepler-1647 desert planet models with a semi-major axis of 1.95 au (black lines), 2.00 au (blue lines), 2.30 au (green lines), and 2.35 au (red lines). Note that there is no significant precipitation in any of these models.

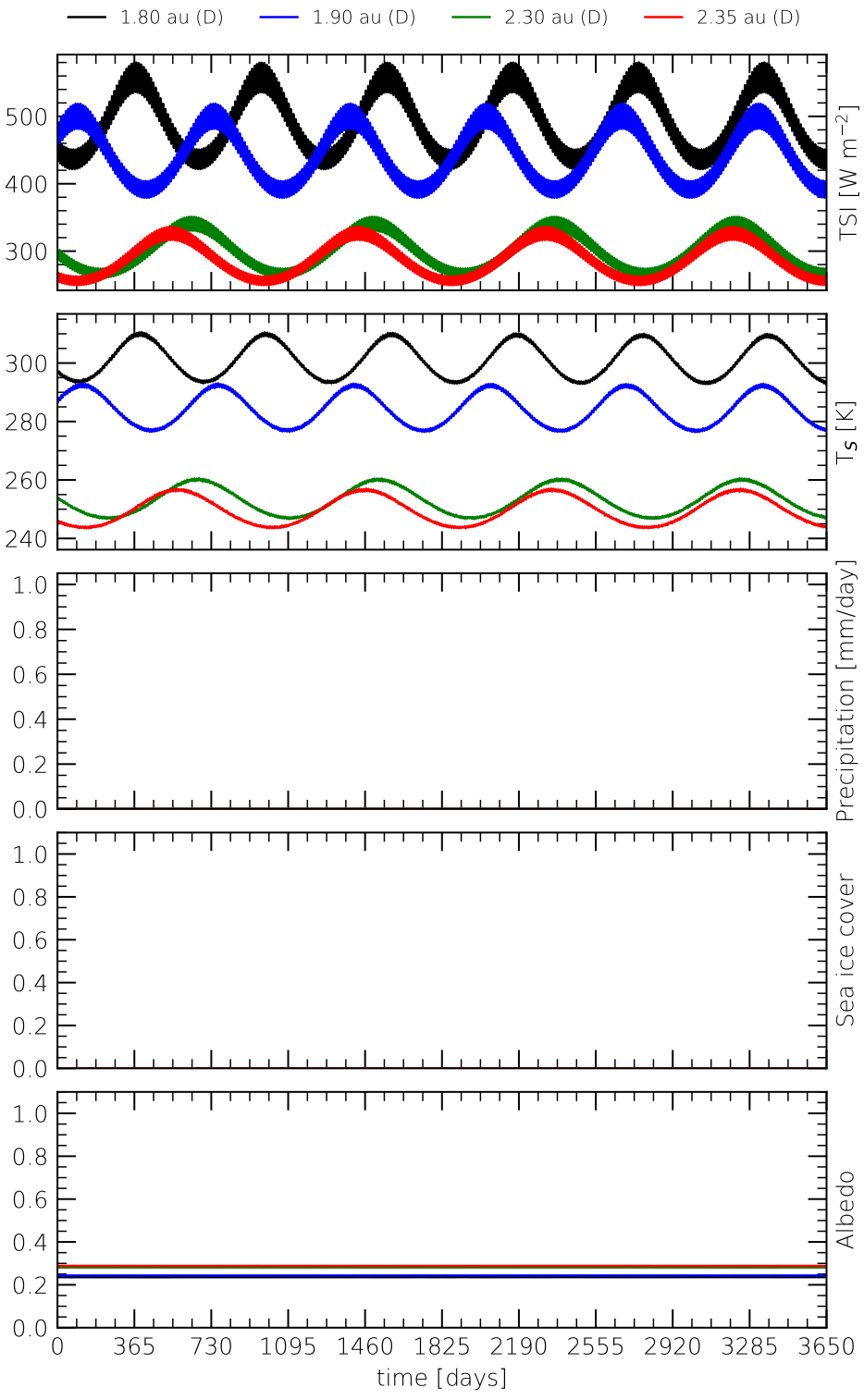

Figure 20: As in Fig. 18, but for the desert planet models presented in Fig. 19. There is no precipitation and sea ice cover in any of these models. Note that the time series of the effective albedo are overlapped.

desert planet are very similar among different semi-major axes. That is, there is no significant amount of precipitation in any of these models, and the cloud cover and effective albedo have in all four models their peak in the polar regions, where snow is slowly accumulated over time. Furthermore, Fig. 20 demonstrates that the precipitation and effective albedo does not vary in any of the four models, while the surface temperature exhibits in each model the long-periodic signal of the TSI. Please note that this is very similar to the temperature variation of the aqua-planet in Snowball state (see Fig. 18). All desert planet models of this study are summarized in table 8.

Figure 21 shows the same as Fig. 17, but for a desert planet with a semi-major axis of 1.80 au (moist Greenhouse state) as well as 1.90 au (habitable state). In the moist Greenhouse state, the specific humidity is well below 0.1 g kg^{-1} at all latitudes

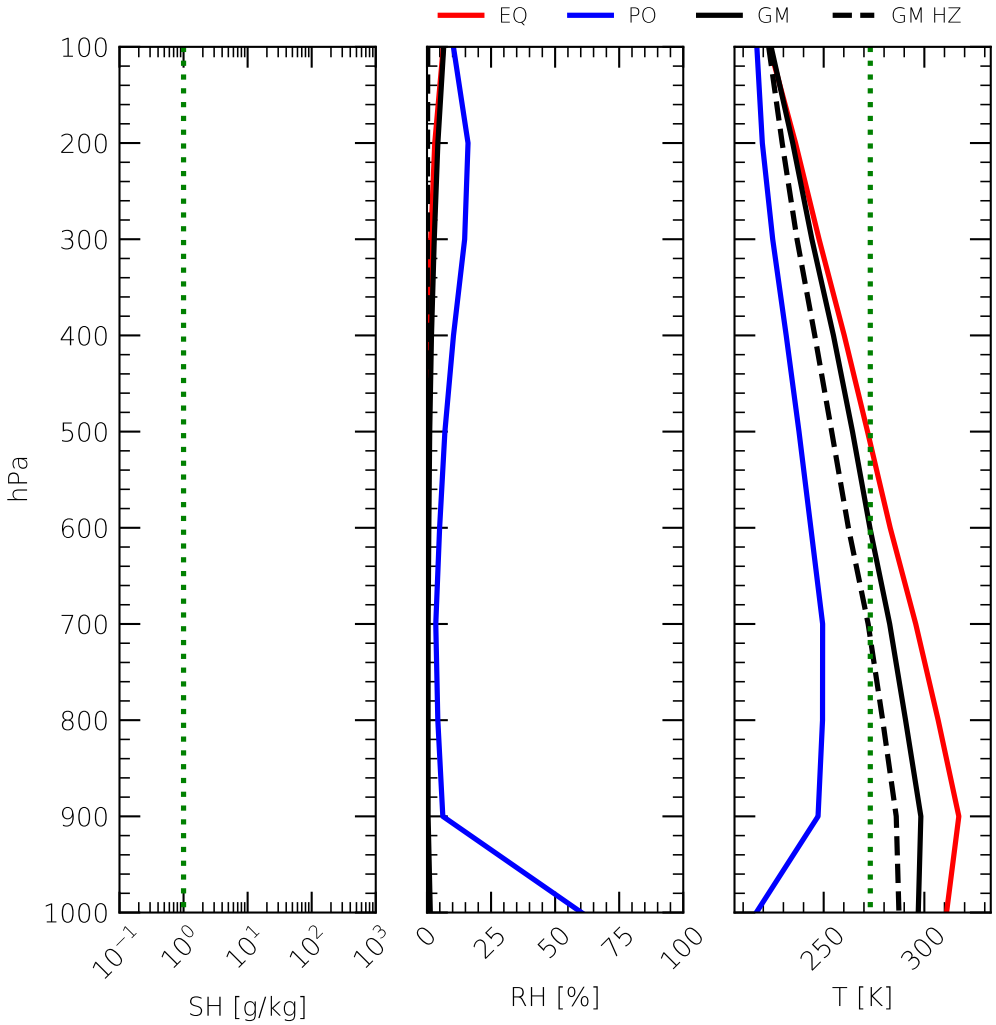

Figure 21: As in Fig. 17, but for a desert planet in the moist Greenhouse state at 1.80 au (solid lines). The dashed lines refer to a desert planet in the habitable zone at 1.90 au. In both cases the specific humidity is below 0.1 g kg^{-1} and the globally averaged relative humidity is close to zero.

Model	Period [days]	TSI [W m^{-2}]	T_S [K]	Precip. [mm/day]	Sea ice cover	Albedo
1.80 au	596	1961.00	300.73	0.00	0.00	0.24
1.90 au	646	1774.55	284.48	0.00	0.00	0.24
2.14 au	773	1380.69	263.90	0.00	0.00	0.26
2.30 au	861	1196.04	252.87	0.00	0.00	0.28
2.35 au	889	1149.24	249.65	0.00	0.00	0.29

Table 8: As in table 7, but for all desert planet models in the Kepler-1647 system.

and heights emphasizing the very dry atmosphere of the planet. The relative humidity shows that the poles are indeed the most humid regions where water is also stored in the form of vapor and clouds. The vertical temperature profile of the polar region shows a relatively strong inversion below 900 hPa, which indicates that the increased cloud cover in this region comes from ground-near fog below the inversion cap. Global maps of cloud cover and relative humidity at 1000 hPa (Fig. 22) reveal that this is indeed the case. At 1.90 au, SH is also below 0.1 g kg^{-1} and RH is almost zero at all heights. That is, there is almost no water vapor in the atmosphere of a habitable desert planet. The temperature profile is similar to that in the moist Greenhouse state, but approximately 10 K lower.

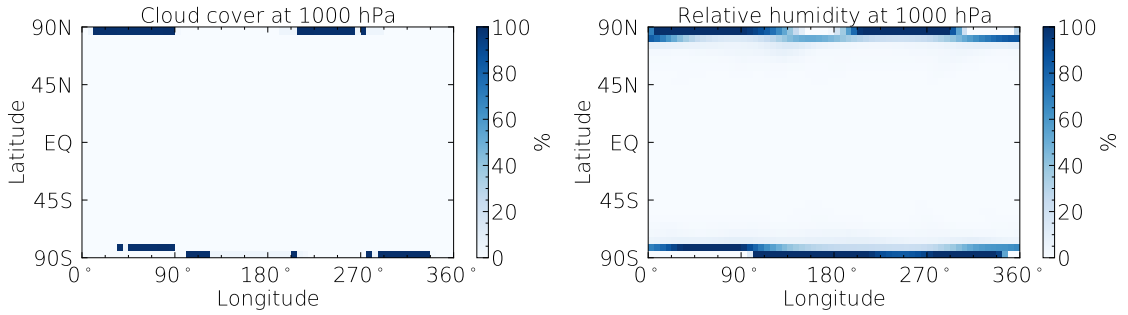

Figure 22: Global maps of the cloud cover and relative humidity at 1000 hPa for a desert planet with a semi-major axis of 1.80 au (moist Greenhouse state). It shows one specific time step during the end of the simulation.

To summarize these studies, the climate states of a planet in the Kepler-1647 system are very similar to those of a planet in Kepler-35, but for different semi-major axes. However, the habitable zone of Kepler-1647 is much wider, and even wider for a desert planet, as already noted by Abe et al. (2011). Furthermore, the temporal variability of the shown quantities are amplified due to the stronger variability of the binary insolation.

4.3 Kepler-47

In this section, an aqua-planet in the Kepler-47 system with a semi-major axis of between 0.83 and 0.885 au is investigated. Results are shown in Figs. 23, 24, and 25 and are presented in the same way as in the previous studies. A planet with a semi-major axis of 0.83 au is in the moist Greenhouse state, with a specific humidity of $\sim$2 g kg^{-1} in the stratosphere (Fig. 23), whereas it is habitable between around 0.835 and 0.88 au. At 0.885 au, the planet then goes into a Snowball state where full glaciation takes place (Fig. 24).

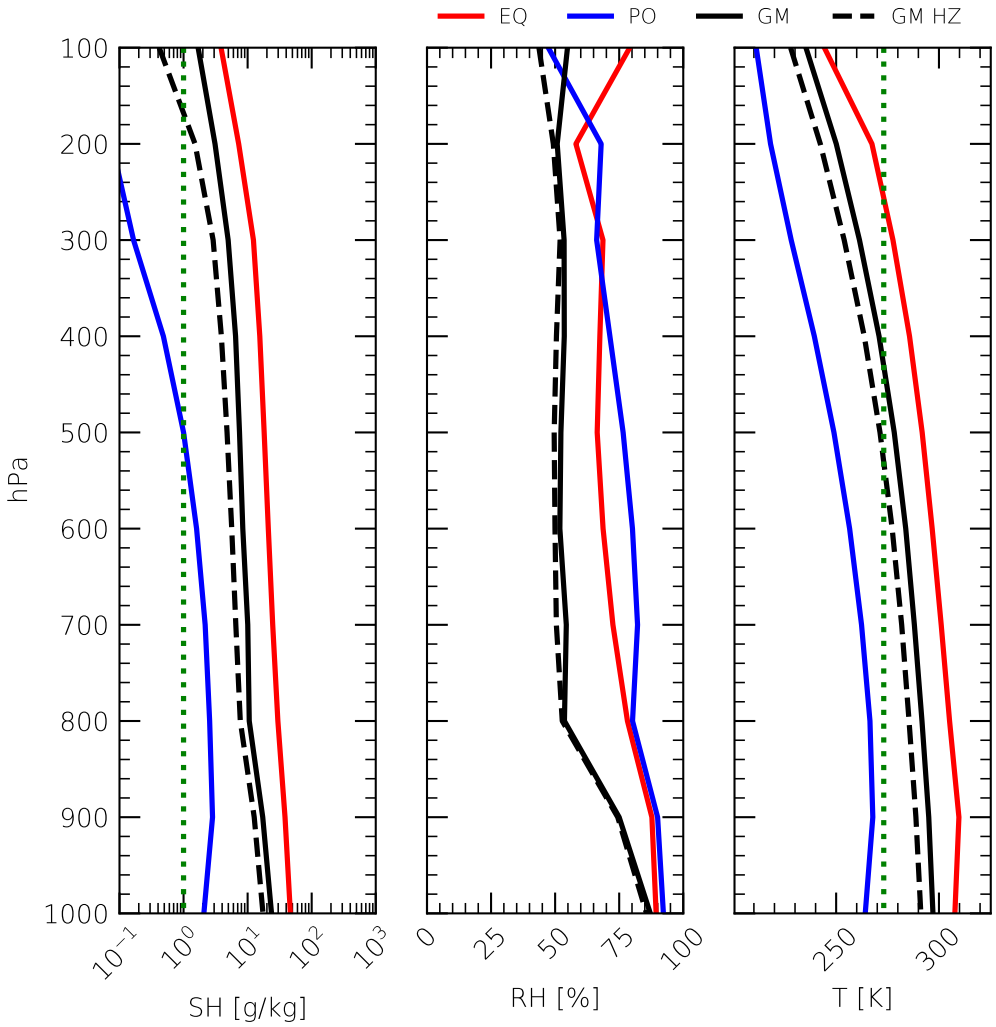

Figure 23: As in Fig. 10, but for a planet in Kepler-47 with a semi-major axis of 0.83 au (solid lines; moist Greenhouse state) and 0.835 au (dashed lines; habitable state).

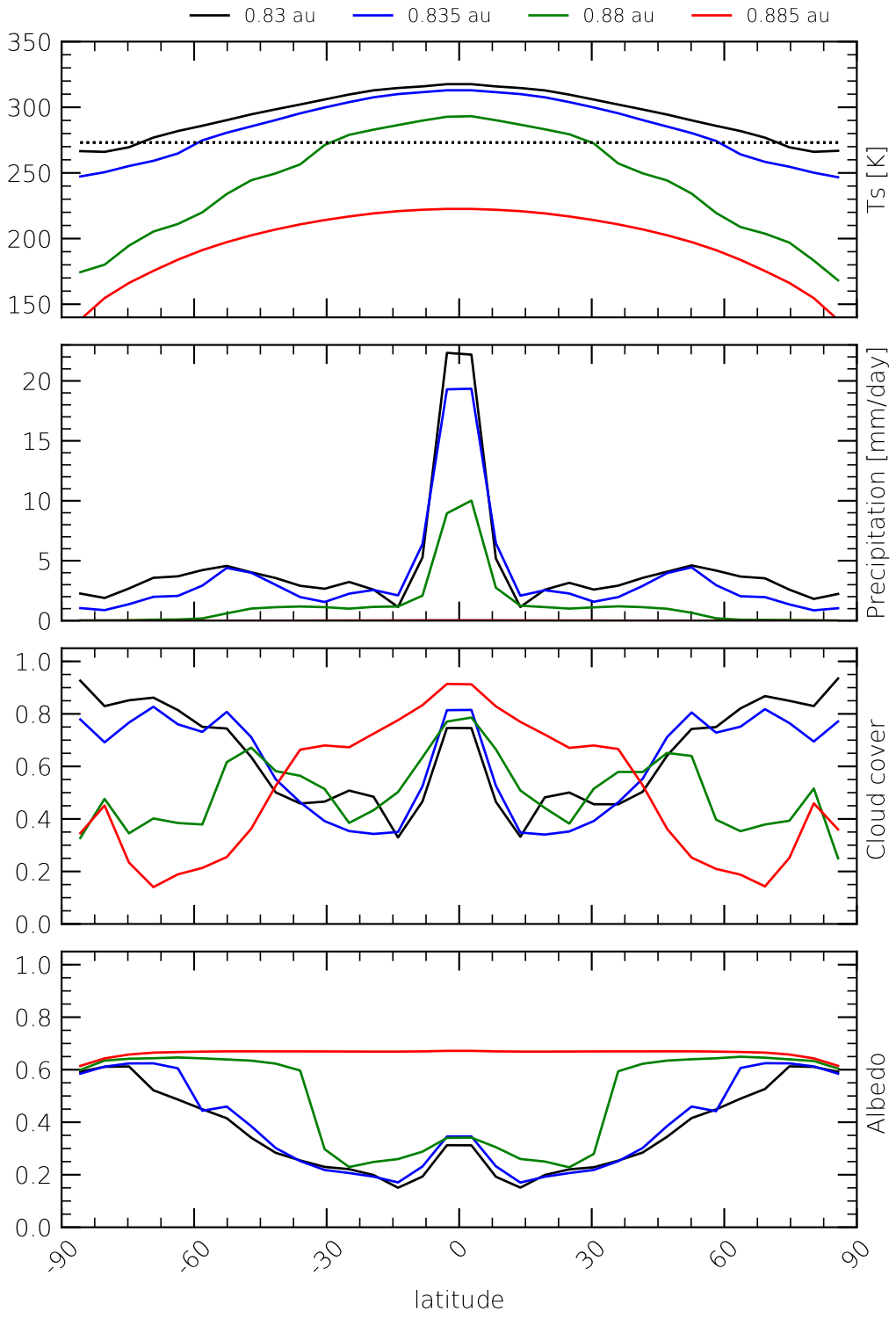

Figure 24: As in Fig. 11, but for an aqua-planet in the Kepler-47 binary system with a semi-major axis of 0.83 au (black solid line), 0.835 au (blue line), 0.88 au (green line), and 0.885 au (red line).

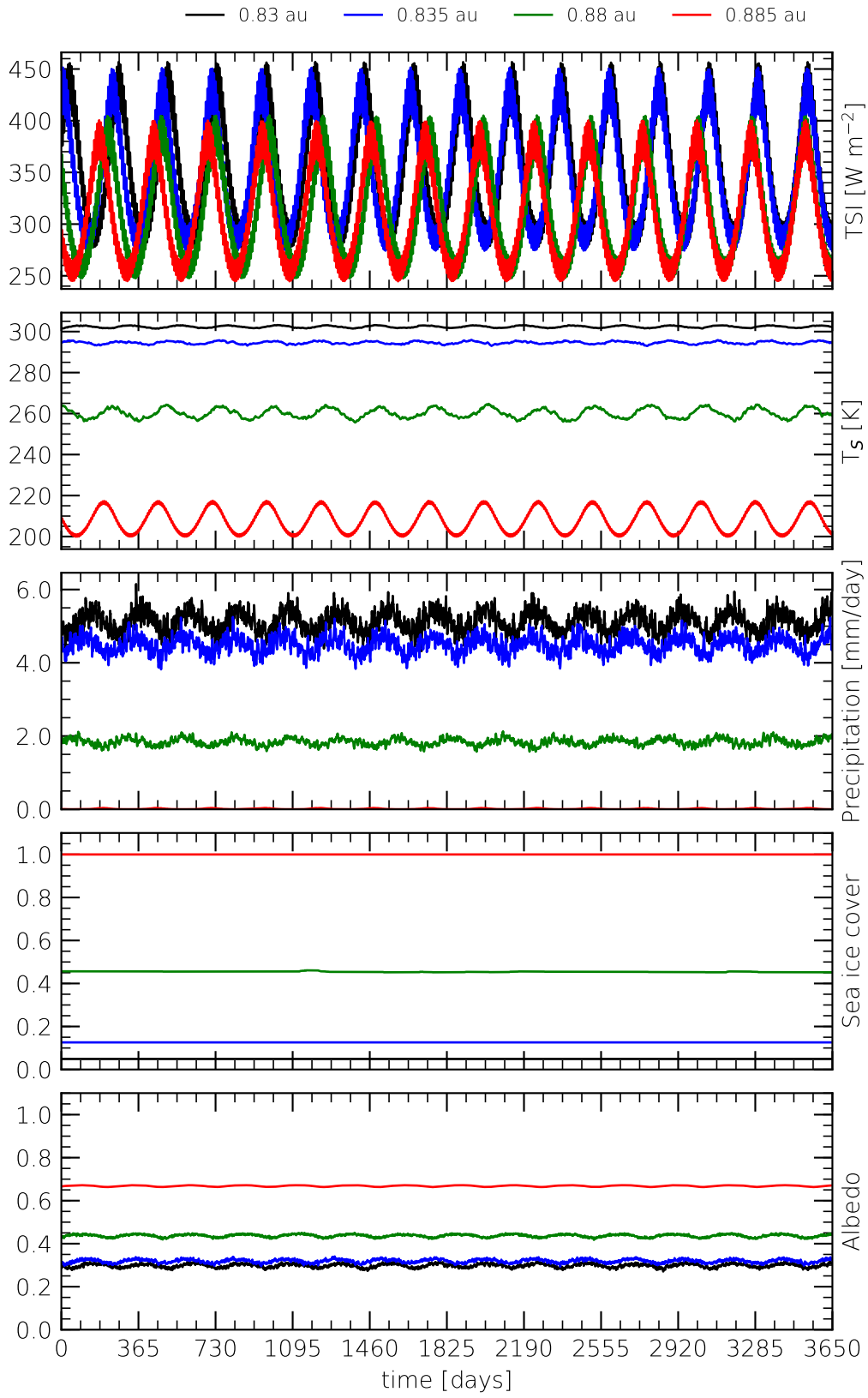

Figure 25: As in Fig. 18, but for the Kepler-47 models presented in Fig. 24.

Again, there is no precipitation but a very high cloud cover in the Snowball state. Apart from different semi-major axes, these results are similar to those of the aforementioned studies (e.g., see Fig. 11 and 16), and thus need no further discussion. For the sake of completeness, corresponding time series are plotted in Fig. 25. Table 9 summarizes globally averaged quantities of the four models presented in this study.

Model	Period [days]	TSI [W m^{-2}]	T_S [K]	Precip. [mm/day]	Sea ice cover	Albedo
0.830 au	233	1414.65	302.38	5.12	0.05	0.30
0.835 au	235	1398.64	294.61	4.49	0.13	0.32
0.880 au	254	1249.27	260.18	1.84	0.45	0.44
0.885 au	257	1236.99	207.94	0.01	1.00	0.67

Table 9: List of orbital periods, total solar insolation TSI as well as globally averaged precipitation, sea ice cover and effective albedo of all Kepler-47 models presented in Fig. 24.

5 Final Remarks

5.1 Discussion

In this thesis, I modified the radiative transfer module of the PlaSim climate model allowing to simulate the climate of circumbinary planets. For that purpose, an additional binary star module is implemented in the existing code, which numerically integrates the 2-body problem with a semi-implicit Euler scheme and calculates the stellar brightness of each individual star based on their mass and temperature. The radiation at the top of the atmosphere, or total solar insolation, is then calculated using simple geometrical considerations. The code can still be executed in a parallel environment, and stellar and orbital parameters are read from an external text file as it is done with other input parameters. In addition to PlaSim's standard output, the total solar insolation as well as orbital parameters of the binary are saved as output.

To investigate the outcome of the modified PlaSim code, I simulated exoplanets in various circumbinary systems. The Kepler-35 system is used to investigate the impact of the binary on the climate, and for a model evaluation where results are compared with those from PE17. A comparison between aqua- and desert-planet HZ limits are performed using the Kepler-1647 system. Furthermore, a planet in the Kepler-47 system is simulated to compare its climate states with those of the planets in the two other systems. The main results of this thesis are the following:

- The Kepler-35 habitable zone limits derived from PlaSim simulations agree relatively well with those found by Popp and Eggl (2017), although they used a different model.
- The binary star can amplify the temporal variability of various climate indicators, such as the globally averaged surface temperature. If this is the case, the amplitude changes with the planetary semi-major axis.
- The habitable zone of a desert planet is much wider than that of an aqua-planet, whereas the temporal variability of the desert planet's surface temperature is very similar to that of an aqua-planet in uninhabitable state.
- While the temporal variability of various climatic indicators heavily depends on the variation of the TSI and the planetary semi-major axis, mean climatic states of the examined planets are very similar among the three systems, even though the semi-major axes are different.

The ECHAM6 model that has been used by Popp and Eggl (2017) has a different complexity and uses other parametrization schemes than PlaSim. I will not discuss these differences due to the complexity of this topic, but I will do a brief comparison between my model setup and that of PE17. First, PE17 carried out simulations with a spatial resolution of 3.75° (compared to 5.6°) using 47 vertical levels up to a pressure of 0.01 hPa (compared to 10 vertical levels up to 100 hPa), which makes the assessment of the stratospheric water vapor easier and more reliable. Moreover, their radiative transfer scheme consists of 14 shortwave bands, instead of one. This

could also has an effect on the outcome. While PE17 used a threshold of 3 g kg^{-1} specific humidity for the transition to the moist Greenhouse state, I used 1 g kg^{-1} as proposed by Kasting (1988). Nonetheless, the resulting HZ limits for Kepler-35 does not change when using the threshold from PE17 (see the solid black line in Fig. 10). In the other two systems (see Figs. 17 and 23), the HZ limits would indeed change marginally. What could actually be a problem is the number of vertical levels that has been used to infer the water vapor content in the stratosphere. As mentioned above, only 10 vertical levels are used, with the uppermost being at 100 hPa. This corresponds to an altitude of roughly 15 km, whereas the stratosphere of an Earth-like atmosphere normally ranges from roughly 12 km to 50–60 km height. That is, the 100 hPa layer is at the bottom of the stratosphere, which might be too low to determine hydrogen escape from the atmosphere. Thus, considering the water vapor content from the upper stratosphere (10 hPa and above) as well would require at least ten times as many vertical levels, given that the height of the uppermost layer of PlaSim is defined by the ratio between surface pressure (usually 1000 hPa) and the number of vertical levels. Furthermore, it should also kept in mind that spatio-temporal averages of the specific humidity are used as threshold for the transition to the moist Greenhouse state. The actual amount of water vapor content in the stratosphere can thus vary in space and time and, consequently, the inferred HZ limits should also be considered as temporal averages. Nonetheless, the modified PlaSim code provides HZ limits for Kepler-35 that agree well with those found by PE17 (see table 10). The PlaSim climate model gives slightly wider HZ limits. I also find that the binary stars clearly introduce an additional variability in the globally averaged surface temperature, which is larger at lower surface temperatures, as also stated by PE17.

System	PlaSim HZ Limits		Literature		Observed
	Inner	Outer	Inner	Outer	-
Kepler-35	1.140	1.210	1.165	1.950	0.603
Kepler-1647	2.140	2.240	1.420	2.490	2.721
Kepler-1647 Desert	1.900	2.300	-	-	-
Kepler-47	0.835	0.880	0.990	1.750	0.296 0.989 0.699

Table 10: Summary of various habitable zone limits for Kepler-35, Kepler-1647, and Kepler-47. PlaSim HZ limits are derived in this study. Literature values are taken from PE17 for Kepler-35, and from Pilat-Lohinger et al. (2019) for Kepler-1647 and Kepler-47 (based on the formulas from Kopparapu et al. (2014) and Haghighipour and Kaltenegger (2013)). Estimated planetary semi-majors axes of observed exo-planets are taken from Welsh et al. (2012), Kostov et al. (2016), Orosz et al. (2012), and Orosz et al. (2019).

For Kepler-1647 and Kepler-47, no HZ limits derived from fully three-dimensional climate model simulations are available in the literature. Instead, table 10 summarizes the analytically calculated HZ limits using the formulas from Kopparapu et al. (2014) and Haghighipour and Kaltenegger (2013). I find that the Kepler-1647 habitable zone derived from PlaSim simulations is substantially smaller but lie well within the limits from the literature, even for a desert planet. In the case of Kepler-47, however, the HZ limits are much closer to the binary than those from the literature. Please note that these HZ limits are well beyond the inner stability limit of their binaries. The stability limit of the Kepler-35 system is at 0.52 au (Chavez et al. 2014), that of Kepler-1647 is at 0.37 au (Kostov et al. 2016), and that of Kepler-47 is at 0.18 au (Quarles et al. 2018). The inferred habitable zones are therefore in all three systems well within the stable region. Moreover, there are no concrete reference values for the HZ limits of a circumbinary desert planet, but the desert planet simulations in this thesis underline the findings by Abe et al. (2011). The HZ limits for dry planets are significantly wider than those of an aqua-planet analogue. The habitable zone for an aqua-planet in the Kepler-1647 system ranges from 2.14 to 2.24 au, while that for a desert planet ranges from 1.90 to 2.30 au. This is a 400 % wider habitable zone for the desert planet. Again, one problem might be that the net solar insolation is highly variable, whereas spatio-temporal averages are used to define the transition to the uninhabitable state. That is, the HZ limits are also considered as temporal averages. As mentioned in the introduction, no terrestrial planet has been observed so far. Even if we assume that the planet under investigation is a natural satellite of one of the observed exoplanets, none of them would actually be habitable (see table 10). Nonetheless, considering the relatively well agreement of the inferred HZ limits with those from the literature, this work suggests that also simplified climate models can provide useful results comparable with those from more complex climate models.

The mean climate states are in all three systems very similar, e.g., surface temperature and precipitation has their maximum at the equator and are relatively small at high latitudes. The total cloud cover peaks in the equator region as well as at high latitudes and has its minimum in subtropical latitudes, and the effective albedo has its maximum at the poles due to glaciation and is relatively low at lower latitudes. These are patterns that are expected from an Earth-like climate model and do not require any further discussion. Nonetheless, the reason for the remarkably large cloud cover in the Snowball state is unclear and needs further investigation of model parameterizations. What is, however, significantly different in each system is the temporal evolution and variability of the aforementioned climate indicators (i.e., climate variability), which is caused by the different strength and amplitude of the TSI. In cold climate states, an additional variability (mainly of the surface temperature), with a period of several days to weeks, is induced by the short-periodic signal of the TSI (caused by the motion of the binary around its center of mass). Other quantities, like precipitation and sea-ice cover, seem to be more insensitive against these short-periodic changes. In warmer states, this effect is minimal and only the long-periodic signal (caused by the eccentric motion of the planet) is present, if at all. Furthermore, it should also be mentioned that only 80 years are simulated,

which is more like a snapshot of the planet's current climatic conditions. On larger timescales, several other mechanisms effecting the climate of a planet become important , e.g. the Milankovitch cycles, resonances with other planets, or even the stellar evolution. In summary it can only be said, therefore, that the binary star induces additional short-term changes (i.e., with periods of several days or weeks) while long-term climate conditions of a planet are relatively unaffected by it.

The most important limitations of the modified PlaSim code are already summarized in section 2. At this point, I want to discuss further consequences of these limitations and other numerical issues. First and foremost, focusing only on circumbinary planets severely limits the number of planets that can be investigated. So far, about hundred planet-hosting binary systems are observed and only 21 of them are circumbinary systems (Schwarz et al. 2016). Another severe restriction is that the atmospheric composition in PlaSim is assumed to be Earth-like, which can not be changed except for the CO_2 concentration. Again, none of the observed circumbinary planets are terrestrial, and no exomoons are observed so far, as it is assumed in this thesis. This really limits the use of the modified PlaSim code I have presented here to theoretical investigations. Furthermore, only binary pairs of the same spectral type can be simulated with that code (even though the investigated binary systems have different spectral types, which may also affect the results) further limiting the number of systems that can be investigated. Nonetheless, Pilat-Lohinger et al. (2019) have shown that the majority of observed binaries are indeed of the same spectral type, if the spectral types interesting for habitability (F, G, K and M) are considered. A technical limitation is constituted by numerical instabilities in the upper atmosphere that occur when the total solar insolation becomes too large, which is the case for a desert planet in the Kepler-1647 system with a semi-major axis of 1.65 au. In order to solve this problem some major revisions of the parameterization schemes might be necessary.

The model I have presented in this thesis is very simplified and thus I want to finalize this work with a future outlook. Subsequent work could, in the first place, imply the integration of the binary routines in a more complex climate model due to the aforementioned limitations of the PlaSim climate model. The problem is that the binary routines I have presented here are customized for the PlaSim climate model. That is, I have not implemented a general interface or wrapper which handles the communication between PlaSim's radiative transfer code and the binary routines. So far, only the true longitude λ and the eccentricity factor are passed from PlaSim to the binary routines and transformed to parameters that are required to calculate the binary insolation. A wrapper would transform all kinds of orbital parameters depending on what is used by the climate model. Also, a module-based code could make the implementation easier and would require only a few minor changes in the climate model code. Furthermore, the presented code is restricted to binaries of the same spectral type. Thus, future work could also imply the revision of PlaSim's radiative transfer code, especially the cloud-radiation interactions, such that binaries with different spectral types can be considered as well.

5.2 Acknowledgments

First and foremost, I would like to acknowledge my co-supervisor for the numerous Skype sessions, his suggestions, and, of course, for his patience over the last two years. It took me an exceptionally long time to finish this thesis as it was done alongside my PhD.

Furthermore, I would like to thank my colleagues from the Institute of Meteorology and Geophysics for some general discussions that helped me from time to time, and for their understanding doing another Master's degree. I would also like to thank my family and friends supporting me in a variety of ways, albeit unknowingly.

6 References

Abbot, Dorian S., Jonah Bloch-Johnson, Jade Checlair, Navah X. Farahat, R. J. Graham, David Plotkin, Predrag Popovic, and Francisco Spaulding-Astudillo. "Decrease in Hysteresis of Planetary Climate for Planets with Long Solar Days". In: *The Astrophysical Journal* 854.1, 3 (2018), p. 3.

Abe, Yutaka, Ayako Abe-Ouchi, Norman Sleep, and Kevin Zahnle. "Habitable Zone Limits for Dry Planets". In: *Astrobiology* 11 (June 2011), pp. 443–60.

Armstrong, D. J., H. P. Osborn, D. J. A. Brown, F. Faedi, Y. Gómez Maqueo Chew, D. V. Martin, D. Pollacco, and S. Udry. "On the abundance of circumbinary planets". In: *Monthly Notices of the Royal Astronomical Society* 444 (Oct. 2014), pp. 1873–1883.

Berger, AndréL. "Long-Term Variations of Daily Insolation and Quaternary Climatic Changes". In: *Journal of the Atmospheric Sciences* 35.12 (1978), pp. 2362–2367.

Chavez, C. E., N. Georgakarakos, S. Prodan, M. Reyes-Ruiz, H. Aceves, F. Betancourt, and E. Perez-Tijerina. "A dynamical stability study of Kepler Circumbinary planetary systems with one planet". In: *Monthly Notices of the Royal Astronomical Society* 446.2 (Nov. 2014), pp. 1283–1292.

Correia, A. C. M., S. Udry, M. Mayor, J. Laskar, D. Naef, F. Pepe, D. Queloz, and N. C. Santos. "The CORALIE survey for southern extra-solar planets. XIII. A pair of planets around HD 202206 or a circumbinary planet?" In: *Astronomy and Astrophysics* 440 (Sept. 2005), pp. 751–758.

Cukier, Wolf, Ravi kumar Kopparapu, Stephen R. Kane, William Welsh, Eric Wolf, Veselin Kostov, and Jacob Haqq-Misra. "Habitable Zone Boundaries for Circumbinary Planets". In: *Publications of the Astronomical Society of the Pacific* 131.1006 (2019), p. 124402.

Duquennoy, A. and M. Mayor. "Multiplicity among solar-type stars in the solar neighbourhood. II - Distribution of the orbital elements in an unbiased sample". In: *Astronomy and Astrophysics* 248 (Aug. 1991), pp. 485–524.

Dvorak, R. "Critical orbits in the elliptic restricted three-body problem." In: *Astronomy and Astrophysics* 167 (1986), pp. 379–386.

Eggenberger, A. and S. Udry. "Probing the Impact of Stellar Duplicity on Planet Occurrence with Spectroscopic and Imaging Observations". In: (2007).

Eggl, Siegfried, Elke Pilat-Lohinger, Nikolaos Georgakarakos, Markus Gyergyovits, and Barbara Funk. "An Analytic Method to Determine Habitable Zones for S-Type Planetary Orbits in Binary Star Systems". In: *The Astrophysical Journal* 752.1, 74 (2012), p. 74.

Gyergyovits, M., S. Eggl, E. Pilat-Lohinger, and Ch. Theis. "Disc-protoplanet interaction - Influence of circumprimary radiative discs on self-gravitating proto-

planetary bodies in binary star systems". In: *Astronomy and Astrophysics* 566 (2014), A114.

Haghighipour, Nader and Lisa Kaltenegger. "Calculating the Habitable Zone of Binary Star Systems. II. P-type Binaries". In: *The Astrophysical Journal* 777.2, 166 (Nov. 2013), p. 166.

Harrington, R. S. "Production of triple stars by the dynamical decay of small stellar systems." In: *The Astronomical Journal* 80 (1975), pp. 1081–1086.

— "Planetary orbits in binary stars." In: *The Astronomical Journal* 82 (1977), pp. 753–756.

Hart, Michael H. "Habitable Zones about Main Sequence Stars". In: *Icarus* 37.1 (1979), pp. 351–357.

Hays, L. E., M. H. New, and M. A. Voytek. "2015 NASA Astrobiology Strategy Document and the Vision for Solar System Exploration". In: *Planetary Science Vision 2050 Workshop*. Vol. 1989. Feb. 2017, p. 8141.

Holman, Matthew J. and Paul A. Wiegert. "Long-Term Stability of Planets in Binary Systems". In: *The Astronomical Journal* 117.1 (1999), pp. 621–628.

Huang, Su-Shu. "The Problem of Life in the Universe and the Mode of Star Formation". In: *Publications of the Astronomical Society of the Pacific* 71 (1959), p. 421.

Huang, Su-Shu. "Life-Supporting Regions in the Vicinity of Binary Systems". In: *PASP* 72.425 (Apr. 1960), p. 106.

Kaltenegger, Lisa and Nader Haghighipour. "Calculating the Habitable Zone of Binary Star Systems. I. S-type Binaries". In: *The Astrophysical Journal* 777.2, 165 (Nov. 2013), p. 165.

Kasting, J. F. "Runaway and moist greenhouse atmospheres and the evolution of Earth and Venus". In: *Icarus* 74.3 (June 1988), pp. 472–494.

Kasting, J. F., J. B. Pollack, and T. P. Ackerman. "Response of Earth's atmosphere to increases in solar flux and implications for loss of water from Venus". In: *Icarus* 57.3 (1984), pp. 335–355.

Kasting, James F., Daniel P. Whitmire, and Ray T. Reynolds. "Habitable Zones around Main Sequence Stars". In: *Icarus* 101.1 (1993), pp. 108 –128.

Kopparapu, Ravi Kumar, Ramses M. Ramirez, James SchottelKotte, James F. Kasting, Shawn Domagal-Goldman, and Vincent Eymet. "Habitable Zones around Main-sequence Stars: Dependence on Planetary Mass". In: *The Astrophysical Journal Letters* 787.2, L29 (2014), p. L29.

Kostov, Veselin B. et al. “Kepler-1647b: The Largest and Longest-period Kepler Transiting Circumbinary Planet”. In: *The Astrophysical Journal* 827.1, 86 (Aug. 2016), p. 86.

Lissauer, J. J. “Planet formation”. In: *Annual Review of Astronomy and Astrophysics* 31 (1993), pp. 129–174.

Lucarini, V., S. Pascale, R. Boschi, E. Kirk, and N. Iro. “Habitability and Multistability in Earth-like Planets”. In: *Astronomische Nachrichten* 334.6 (2013), p. 576.

Lunkeit, Frank, Simon Blessing, Klaus Fraedrich, Heiko Jansen, Edilbert Kirk, Ute Luksch, and Frank Sielmann. “Planet Simulator”. In: (2004).

Martin, David V. “Populations of Planets in Multiple Star Systems”. In: *Handbook of Exoplanets*. Cham: Springer International Publishing AG, 2018, pp. 1–26.

Mathieu, R. D., A. M. Ghez, E. L. N. Jensen, and M. Simon. “Young Binary Stars and Associated Disks”. In: *Protostars and Planets IV* (May 2000), p. 703.

Mayor, M. and D. Queloz. “A Jupiter-mass companion to a solar-type star”. In: *Nature* 378 (Nov. 1995), pp. 355–359.

Menou, Kristen. “Water-trapped Worlds”. In: *The Astrophysical Journal* 774.1, 51 (2013), p. 51.

Moorman, S. Y., B. L. Quarles, Zh. Wang, and M. Cuntz. “The habitable zone of Kepler-16: impact of binarity and climate models”. In: *International Journal of Astrobiology* 18.1 (Feb. 2019), pp. 79–89.

Orosz, Jerome A. et al. “Kepler-47: A Transiting Circumbinary Multiplanet System”. In: *Science* 337.6101 (2012), p. 1511.

Orosz, Jerome A. et al. “Discovery of a Third Transiting Planet in the Kepler-47 Circumbinary System”. In: *The Astronomical Journal* 157.5, 174 (May 2019), p. 174.

Paradise, Adiv, Bo Lin Fan, Kristen Menou, and Christopher Lee. “Climate Diversity in the Habitable Zone due to Varying pN_2 Levels”. In: *Astrophysics - Earth and Planetary Astrophysics* (2019).

Perryman, Michael. *The Exoplanet Handbook*. Cambridge University Press, 2011.

Pilat-Lohinger, E., B. Funk, and R. Dvorak. “Stability limits in double stars. A study of inclined planetary orbits”. In: *Astronomy and Astrophysics* 400 (2003), pp. 1085–1094.

Pilat-Lohinger, Elke and Rudolf Dvorak. “Stability of S-type Orbits in Binaries”. In: *Celest. Mech. Dyn. Astron.* 82 (Feb. 2002), pp. 143–153.

Pilat-Lohinger, Elke, Siegfried Eggl, and Akos Bazso. *Planetary Habitability In Binary Systems*. Advances In Planetary Science. World Scientific Publishing Company, 2019.

Popp, Max and Siegfried Eggl. "Climate variations on Earth-like circumbinary planets". In: *Nature communications*. Apr. 2017.

Quarles, B., S. Satyal, V. Kostov, N. Kaib, and N. Haghighipour. "Stability Limits of Circumbinary Planets: Is There a Pile-up in theKeplerCBPs?" In: *The Astrophysical Journal* 856.2 (2018), p. 150.

Quintana, E. V., F. C. Adams, J. J. Lissauer, and J. E. Chambers. "Terrestrial Planet Formation around Individual Stars within Binary Star Systems". In: *The Astrophysical Journal* 660 (May 2007), pp. 807–822.

Rabl, G. and R. Dvorak. "Satellite-type planetary orbits in double stars : a numerical approach." In: *Astronomy and Astrophysics* 191 (1988), pp. 385–391.

Raghavan, Deepak et al. "A survey of stellar families: Multiplicity of solar-type stars". In: *The Astrophysical Journal Supplement Series* 190.1 (2010), pp. 1–42.

Safronov, V.S. *Evolution of the protoplanetary cloud and formation of the earth and the planets*. NASA technical translation. Israel Program for Scientific Translations, 1972.

Schwarz, R., B. Funk, R. Zechner, and Á. Bazsó. "New prospects for observing and cataloguing exoplanets in well-detached binaries". In: *Monthly Notices of the Royal Astronomical Society* 460.4 (May 2016), pp. 3598–3609.

Shields, Aomawa L., Victoria S. Meadows, Cecilia M. Bitz, Raymond T. Pierrehumbert, Manoj M. Joshi, and Tyler D. Robinson. "The Effect of Host Star Spectral Energy Distribution and Ice-Albedo Feedback on the Climate of Extrasolar Planets". In: *Astrobiology* 13.8 (2013), pp. 715–739.

Stevens, Bjorn et al. "Atmospheric component of the MPI-M Earth System Model: ECHAM6". In: *Journal of Advances in Modeling Earth Systems* 5.2 (2013), pp. 146–172.

Szebehely, V. "Stability of Planetary Orbits in Binary Systems". In: *Celestial Mechanics* 22.1 (1980), pp. 7–12.

Tian, Z.-J. et al. "Binary Star Fractions from the LAMOST DR4". In: *Research in Astronomy and Astrophysics* 18 (May 2018), p. 052.

Way, M. J., Anthony D. Del Genio, Igor Aleinov, Thomas L. Clune, Maxwell Kelley, and Nancy Y. Kiang. "Climates of Warm Earth-like Planets. I. 3D Model Simulations". In: *The Astrophysical Journal Supplement Series* 239.2 (2018), p. 24.

Welsh, W. F., J. A. Orosz, J. A. Carter, and D. C. Fabrycky. "Recent Kepler Results On Circumbinary Planets". In: *Formation, Detection, and Characterization of*

Extrasolar Habitable Planets. Ed. by N. Haghighipour. Vol. 293. IAU Symposium. Apr. 2014, pp. 125–132.

Welsh, William F. et al. "Transiting circumbinary planets Kepler-34 b and Kepler-35 b". In: *Nature* 481.7382 (Jan. 2012), pp. 475–479.

Wolf, Eric T., Aomawa L. Shields, Ravi K. Kopparapu, Jacob Haqq-Misra, and Owen B. Toon. "Constraints on Climate and Habitability for Earth-like Exoplanets Determined from a General Circulation Model". In: *The Astrophysical Journal* 837.2 (2017), p. 107.

Wolszczan, A. and D. A. Frail. "A planetary system around the millisecond pulsar PSR1257 + 12". In: *Nature* 355 (Jan. 1992), pp. 145–147.

Wordsworth, R. D. and R. T. Pierrehumbert. "Water Loss from Terrestrial Planets with CO_2-rich Atmospheres". In: *The Astrophysical Journal* 778.2, 154 (2013), p. 154.

Wright, J. T., G. W. Marcy, A. W. Howard, John Asher Johnson, T. D. Morton, and D. A. Fischer. "The frequency of hot jupiters orbiting nearby solartype stars". In: *The Astrophysical Journal* 753.2 (2012), p. 160.

A Appendix

A.1 Source Code

This section provides the full binary code and describes how it is implemented in the PlaSim (v3.18.0) climate model. The implementation requires some minor changes of the original PlaSim code (listings 1, 2, 3, and 4), which are important to run the code properly. The binary code itself consists of a module (listing 5), which defines all necessary variables, and multiple subroutines (listings 6, 7, 8, 9, and 10) to initialize the binary code, perform the integration, calculate various angles and distances between binary and planet, and to compute the insolation of each individual star.

In general, the PlaSim code consists of three major parts, which are executed subsequently. The first part is called *prolog* and initializes all important modules at the beginning of a simulation. The second part is called *Master* and contains the main loop performing the integration in time. The third part is called *epilog* and finalizes the simulation. Consequently, the binary code is implemented as follows. First, binary routines are initialized during the initialization of the radiative transfer module (listing 1) at the beginning of a simulation. Here, input variables are read from *binary_namelist* (see listing 11) and initial positions and velocities of the binary are calculated (listing 6). During the main loop, PlaSim's *radstep* routine is executed, which calls the routine *solang* (listing 2) and then *swr* (listing 3). The former computes the declination and zenith angle, and calls the routines *BINARY_Integrate* (listing 7) and *BINARY_Angles* (listing 8) to compute the binary orbits and various angles (declination, zenith and hour angle), respectively. The binary and planet coordinate vectors are calculated in the *BINARY_Distances* routine (listing 9), which is called after the computation of the declination (listing 4). The routine *swr* then calls *BINARY_Insolation* (listing 10) to calculate the insolation of the binary, which is passed back to *swr* replacing PlaSim's insolation variable. The module *BINARY_module* (listing 5) has to be used by all binary routines. Some of the existing comments in the code are removed for the sake of convenience. Modifications of the existing PlaSim code are indicated with 'MODIFICATION'.

```
1  subroutine radini
2       use radmod
3       namelist/radmod_nl/ndcycle,ncstsol,solclat,solcdec,no3,co2 &
4      & ,iyrbp,nswr,nlwr &
5      & ,a0o3,a1o3,aco3,bo3,co3,toffo3,o3scale &
6      & ,nsol,nswrcl,nrscat,rcl1,rcl2,acl2,clgray,tpofmt &
7      & ,acllwr,tswr1,tswr2,tswr3,th2oc,dawn
8
9       ! MODIFICATION: Initialize binary module
10      call BINARY_init()
11
12      jtune=0
13      if(ndheat > 0) then
```

```
14       if(NTRU==21 .or. NTRU==1) then
15 ...
16      return
17 end subroutine radini
```

Listing 1: Modifications in PlaSim's radini routine.

```
1  subroutine solang
2  ...
3       call ntomin(nstep,imin,ihou,iday,imon,iyea)
4  !
5  !** 2) compute declination [radians]
6
7       call orb_decl(zcday, eccen, mvelpp, lambm0, obliqr, zdecl, eccf)
8  !
9       ! MODIFICATION: Binary Integration
10      ! InitAzimuth sets gmu0_S1 and gmu0_S2 to zero
11      call BINARY_Integrate()
12      call BINARY_InitAzimuth()
13
14 !** 3) compute zenith angle
15      gmu0(:) = 0.0
16      zmuz = 0.0
17      zdawn = sin(dawn * PI / 180.0)
18      zrlon = TWOPI / NLON
19      zrtim = TWOPI / 1440.0
20      zmins = ihou * 60 + imin
21      jhor = 0
22      if (ncstsol==0) then
23       do jlat = 1 , NLPP
24        do jlon = 0 , NLON-1
25         jhor = jhor + 1
26         zhangle = zmins * zrtim + jlon * zrlon - PI
27         zmuz=sin(zdecl)*sid(jlat)+cola(jlat)*cos(zdecl)*cos(zhangle)
28         if (zmuz > zdawn) gmu0(jhor) = zmuz
29
30         ! MODIFICATION: Computes angles for binary
31         call BINARY_Angles(obliqr,zmins,zrtim,jlon,jlat,zrlon,jhor,zdawn,
               zdecl,zhangle,gmu0(jhor))
32        enddo
33       enddo
34      else
35       solclatcdec=solclat*solcdec
36       solslat=sqrt(1-solclat*solclat)
37       solsdec=sqrt(1-solcdec*solcdec)
38 ...
39 end subroutine solang
```

Listing 2: Modifications of PlaSim's solang subroutine.

```
subroutine swr
...
      real zb2(NHOR),zom0(NHOR),zuz(NHOR),zun(NHOR),zr(NHOR)
      real zexp(NHOR),zu(NHOR),zb1(NHOR)
!
      logical losun(NHOR)
!
      ! MODIFICATION: define new variables
      integer :: sel_bin
      logical :: tmp_losun(NHOR), bool_zmu1(NHOR)

      if (ndcycle == 0) then
         js = 1
         je = NLON
         do jlat = 1 , NLPP
            icnt = count(gmu0(js:je) > 0.0)
            if (icnt > 0) then
               zsum = sum(gmu0(js:je))
               zmu0(js:je) = zsum / icnt
               zmu1(js:je) = zsum / NLON
            else
               zmu0(js:je) = 0.0
               zmu1(js:je) = 0.0
            endif
            js = js + NLON
            je = je + NLON
         enddo
      else
         zmu0(:) = gmu0(:)
         zmu1(:) = gmu0(:)
      endif

      ! MODIFICATION: Computation of the binary insolation
      call BINARY_sel_bin(sel_bin)
      if (sel_bin.eq.1) then
         ! binary insolation
         call BINARY_Insolation(zftop1,zftop2,zsolar1,zsolar2,gsol0)
      else
         ! single star insolation
         zftop1(:) = zsolar1 * gsol0 * gdist2 * zmu1(:)
         zftop2(:) = zsolar2 * gsol0 * gdist2 * zmu1(:)
      end if

      ! MODIFICATION: Define grid points where insolation > 0
      if (sel_bin.eq.1) then
         tmp_losun(:) = (zftop1(:) + zftop2(:) > zero)
         bool_zmu1(:) = (zmu1(:).gt.zero)
         losun(:) = (tmp_losun(:).and.bool_zmu1(:))
      else
```

```
50          losun(:) = (zftop1(:) + zftop2(:) > zero)
51        end if
52
53  ! cloud properites
54  !
55        zcs(:) = 1.0 ! Clear sky fraction (1.0 = clear sky)
56        zmu00 = 0.5
57        zb3 = tswr1 * SQRT(zmu00) / zmu00
58        zb4 = tswr2 * SQRT(zmu00)
59        zb5 = tswr3 * zmu00 * zmu00
60  ...
61  end subroutine swr
```

Listing 3: Modifications in PlaSim's swr routine.

```
1  subroutine orb_decl(calday,eccen,mvelpp,lambm0,obliqr,delta,eccf)
2  ...
3        delta = asin(sin(obliqr)*sin(lamb))
4        eccf = invrho*invrho
5
6        ! MODIFICATION: calculate Planet-Binary distances
7        call BINARY_Distances(eccf,lamb)
8  return
9  end subroutine orb_decl
```

Listing 4: Modifications in PlaSim's orb_decl routine.

```
1  module BINARY_module
2        use pumamod, only : NHOR
3        implicit none
4
5        ! Constants
6        real*8, parameter :: pi = 3.141592
7        real*8, parameter :: G = 6.67408*10**(-11.0)
8        real*8, parameter :: Msolar = 1.989*1E30
9        real, parameter :: Lsolar = 3.828*1E26
10       real, parameter :: Rsolar = 6.955*1E8
11       real, parameter :: au1 = 1.4959787E11
12       real, parameter :: SBCONST = 5.670373*1E-8
13       real, parameter :: beta_S1 = 4.0
14       real, parameter :: beta_S2 = 4.0
15       real, parameter :: incl1 = 0.0 ! in degree
16       real, parameter :: incl_thresh_occul = 1.0 ! in degree
17
18       ! Variables from namelist
19       integer :: sel_bin
20       integer :: sel_StefanBoltzmann = 0
21       real  :: dt
22       real :: Star1_SolarMass
23       real :: Star2_SolarMass
```

```
24      real :: Star1_SemiMajorAxis
25      real :: Binary_SemiMajorAxis
26      real :: Binary_Eccentricity
27      real :: Planet_SemiMajorAxis
28      real :: R_S1
29      real :: R_S2
30      real :: Temp_S1
31      real :: Temp_S2
32
33      ! Variables to be computed
34      integer :: sign_S1, sign_S2
35      real :: sma
36      real :: com_lamb
37      real :: gsol0_S1, gsol0_S2
38      real :: L_S1, L_S2
39      real :: alpha_S1, alpha_S2
40      real :: dist_S1, dist_S2
41      real :: eccf_S1, eccf_S2
42      real :: occul_S1, occul_S2
43      real :: angle_S1, angle_S2, angle_P
44      real :: A_S1, A_S2
45      real :: apS1C, apS2C
46      real, dimension(2)  :: com, coor_P
47      real, dimension(NHOR) :: gmu0_S1, gmu0_S2
48      real*8 :: mass_S1, mass_S2
49      real*8, dimension(2) :: coor_S1, coor_S2
50      real*8, dimension(2) :: velo_S1, velo_S2
51      real*8, allocatable, dimension(:,:) :: CoorArrayS1, CoorArrayS2
52
53      ! Switchers and counters
54      integer :: cnt_bi
55      real :: cnt_time = 0.
56      real :: cnt_time_single = 0.
57      logical :: switch_insol = .True.
58      logical :: switcher_2b = .True.
59  end module BINARY_module
```

Listing 5: Module for binary routines.

```
1   subroutine BINARY_init()
2       use BINARY_module
3       use pumamod, only : mypid
4       implicit none
5
6       real :: mratio, mu
7
8       ! Output files
9       character(len=200) :: out_2b = 'Binary-Coordinates.out'
10      character(len=200) :: out_log = 'Binary-OrbitalParam.out'
11      character(len=200) :: out_log3 = 'Binary-Angles.out'
```

```
12      character(len=200) :: out_log2 = 'Binary-HourAngle.out'
13      character(len=200) :: out_insol = 'Binary-Insolation.out'
14      character(len=200) :: out_insol_s = 'SingleStarInsolation.out'
15
16      ! Read namelist
17      character(len=200) :: binary_namelist = 'binary_namelist'
18      namelist /binary_nl/ Star1_SolarMass, Star2_SolarMass, &
19           Planet_SemiMajorAxis, Binary_SemiMajorAxis, &
20           Binary_Eccentricity, sel_bin, sel_StefanBoltzmann, &
21           Temp_S1, Temp_S2, R_S1, R_S2, dt
22      open(101,file=binary_namelist)
23      read(101,binary_nl)
24      close(101)
25
26      ! Compute star masses in [kg]
27      mass_S1 =  Star1_SolarMass * Msolar
28      mass_S2 =  Star2_SolarMass * Msolar
29
30      ! Compute planetary semi major axis in [m]
31      sma =   Planet_SemiMajorAxis * au1
32
33      ! Compute semi major axis of primary star
34      Star1_SemiMajorAxis = Binary_SemiMajorAxis/(1 + mass_S1/mass_S2)
35
36      ! Compute initial coordinate of primary star in [m]
37      coor_S1(1)= Star1_SemiMajorAxis * au1 * (1 - Binary_Eccentricity)
38
39      ! Create output files
40      open(unit=96,file=trim(out_insol_s),status='unknown',action='write')
41      open(unit=97,file=trim(out_insol),status='unknown',action='write')
42      open(unit=98,file=trim(out_2b),status='unknown',action='write')
43      open(unit=99,file=trim(out_log),status='unknown',action='write')
44      open(unit=102,file=trim(out_log2),status='unknown',action='write')
45      open(unit=103,file=trim(out_log3),status='unknown',action='write')
46
47      ! Define y position of 1. star and center of mass COM, DO NOT CHANGE
48      coor_S1(2) =  0.0
49      com(1) =   0.0
50      com(2) =   0.0
51
52      ! Compute initial coordinates of 2nd star according to reformulation
            of Center of mass equation
53      coor_s2(1) = com(1)*(mass_S1 + mass_S2)/mass_S2 - (mass_S1/mass_S2)*
           coor_S1(1)
54      coor_s2(2) = com(2)*(mass_S1 + mass_S2)/mass_S2 - (mass_S1/mass_S2)*
           coor_S1(2)
55
56      ! Compute star distances relative to COM in [m]
57      dist_S1 = sqrt((coor_s1(1)-com(1))**2. + (coor_s1(2)-com(2))**2.)
```

```
58      dist_S2 = sqrt((coor_s2(1)-com(1))**2. + (coor_s2(2)-com(2))**2.)
59
60      ! Compute initial velocities
61      mu = G*(mass_S1 + mass_S2)
62      mratio = mass_s2/(mass_s2+mass_s1)
63      velo_s1(1) = 0.
64      velo_s2(1) = 0.
65      velo_s1(2) = sqrt(mu/(Binary_SemiMajorAxis*au1) * (1. +
           Binary_Eccentricity)/(1. - Binary_Eccentricity))* mratio
66      velo_s2(2) = -velo_s1(2)*mass_s1/mass_s2
67
68      ! Compute alpha coefficients
69      if (mass_S1/Msolar.gt.2.0) then
70           alpha_S1 = 3.5
71      else
72           alpha_S1 = 4.0
73      end if
74      if (mass_S2/Msolar.gt.2.0) then
75           alpha_S2 = 3.5
76      else
77           alpha_S2 = 4.0
78      end if
79
80      ! Compute luminosities L/L_sun
81      if (sel_StefanBoltzmann.eq.1) then
82         ! from Stefan-Boltzmann law
83         if (R_S1.eq.0.or.R_S2.eq.0) then
84            print *, "ERROR! RADII NOT DEFINED!"
85            stop
86         end if
87         L_S1 = (4.*pi*SBCONST * (Rsolar*R_S1)**2. * Temp_S1**4.)/Lsolar
88         L_S2 = (4.*pi*SBCONST * (Rsolar*R_S2)**2. * Temp_S2**4.)/Lsolar
89      else
90         ! from mass-luminosity relation
91         L_S1 = (mass_S1/Msolar)**alpha_S1
92         L_S2 = (mass_S2/Msolar)**alpha_S2
93      end if
94
95      ! Compute radius and area for occultation
96      if (R_S1.eq.0.or.R_S2.eq.0) then
97         R_S1 = Rsolar*(mass_S1/Msolar)**((beta_S1-1)/(beta_S1+3))
98         R_S2 = Rsolar*(mass_S2/Msolar)**((beta_S2-1)/(beta_S2+3))
99      else
100        R_S1 = R_S1*Rsolar
101        R_S2 = R_S2*Rsolar
102     end if
103
104     A_S1 = R_S1**2.0 * pi
105     A_S2 = R_S2**2.0 * pi
```

```
106 end subroutine BINARY_init
```

Listing 6: Initialization of binary routines.

```
 1 subroutine BINARY_Integrate()
 2      use BINARY_module
 3      use pumamod, only : n_days_per_year, n_run_years, mypid
 4      implicit none
 5
 6      integer :: i, cnt_store
 7      integer :: TotalSteps, ts1, ts2
 8      real*8 :: r_12
 9
10      if (sel_bin.eq.1) then
11         ! Compute binary orbits at the beginning
12         if (switcher_2b) then
13            ! Check whether dt is valid
14            if (mod(2700,int(dt)).ne.0) then
15               print *, "ERROR! INVALID TIME STEP!"
16               stop
17            end if
18
19            ! Define number of steps
20            ts1 = (24*3600)/dt
21            ts2 = (n_run_years+2)*n_days_per_year
22            TotalSteps = ts1*ts2
23
24            if (TotalSteps.lt.0) then
25               print *, "ERROR! POTENTIAL OVERFLOW ERROR!"
26               stop
27            end if
28
29            allocate(CoorArrayS1(TotalSteps,2))
30            allocate(CoorArrayS2(TotalSteps,2))
31            CoorArrayS1(:,:) = 0.
32            CoorArrayS2(:,:) = 0.
33            cnt_store = 1
34
35            ! SYMPLECTIC EULER (Binary orbit integration)
36            do i = 0,TotalSteps-1
37               r_12 = sqrt((coor_S1(1) - coor_S2(1))**2.0 + (coor_S1(2) -
                     coor_S2(2))**2.0)
38
39               velo_S1(:) = velo_S1(:) - (G*mass_s2*(coor_S1(:) - coor_S2
                     (:)))/(r_12**3.0)*dt
40               velo_S2(:) = velo_S2(:) - (G*mass_S1*(coor_S2(:) - coor_S1
                     (:)))/(r_12**3.0)*dt
41
42               coor_S1(:) = coor_S1(:) + velo_S1(:)*dt
43               coor_S2(:) = coor_S2(:) + velo_S2(:)*dt
```

```
44
45            if (mod(i,2700/int(dt)).eq.0) then
46               CoorArrayS1(cnt_store,:) = coor_S1(:)
47               CoorArrayS2(cnt_store,:) = coor_S2(:)
48               cnt_store = cnt_store + 1
49            end if
50            end do
51
52            ! Coordinates after first integration step
53            cnt_bi = 1
54            coor_S1(1) = CoorArrayS1(cnt_bi,1)
55            coor_S1(2) = CoorArrayS1(cnt_bi,2)
56            coor_S2(1) = CoorArrayS2(cnt_bi,1)
57            coor_S2(2) = CoorArrayS2(cnt_bi,2)
58            cnt_bi = cnt_bi + 1
59            switcher_2b = .False.
60         else
61            ! For subsequent steps, binary orbits are passed to coor_S1/2
62            coor_S1(1) = CoorArrayS1(cnt_bi,1)
63            coor_S1(2) = CoorArrayS1(cnt_bi,2)
64            coor_S2(1) = CoorArrayS2(cnt_bi,1)
65            coor_S2(2) = CoorArrayS2(cnt_bi,2)
66            cnt_bi = cnt_bi + 1
67         end if
68      end if
69 end subroutine BINARY_Integrate
```

Listing 7: Full integration of the binary orbits at the beginning of a simulation.

```
1  subroutine BINARY_Angles(obliq,zmins,zrtim,jlon,jlat,zrlon,jhor,zdawn,
       decl_com,h_com,za_com)
2        use BINARY_module
3        use pumamod, only: sid, cola, mypid, NROOT
4        implicit none
5
6        integer :: jhor, jlon, jlat
7        real :: zmins, zrtim, zrlon, zdawn
8        real :: za_com, decl_com, h_com
9        real :: obliq
10       real :: decl_S1, decl_S2
11       real :: HANGLE_S1, HANGLE_S2
12       real :: angle_zenith_S1, angle_zenith_S2
13       real, parameter :: pi0 = 3.141592
14
15       if (sel_bin.eq.1) then
16          ! Star 1: compute declination, hour angle, zenith angle
17          decl_S1 = asin(sin(obliq)*sin(com_lamb - sign_S1*apS1C))
18          HANGLE_S1 = zmins * zrtim + jlon * zrlon - pi0 - sign_S1*apS1C
19          angle_zenith_S1 = sin(decl_S1)*sid(jlat)+cola(jlat)*cos(decl_S1)*
               cos(HANGLE_S1)
```

```
20
21          ! Define zenith angle only if star 1 is visible
22          if (angle_zenith_S1 > zdawn) gmu0_S1(jhor) = angle_zenith_S1
23
24          ! Star 2: compute declination, hour angle, zenith angle2
25          decl_S2 = asin(sin(obliq)*sin(com_lamb - sign_S2*apS2C))
26          HANGLE_S2 = zmins * zrtim + jlon * zrlon - pi0 - sign_S2*apS2C
27          angle_zenith_S2 = sin(decl_S2)*sid(jlat)+cola(jlat)*cos(decl_S2)*
                cos(HANGLE_S2)
28
29          ! Define zenith angle only if star 2 is visible
30          if (angle_zenith_S2 > zdawn) gmu0_S2(jhor) = angle_zenith_S2
31
32          ! Write output
33          if (mypid.eq.NROOT) then
34             if (jlon.eq.0.and.jlat.eq.4) then
35                write(103,*) cnt_time, sign_S1, sign_S2, apS1C, apS2C,
                      decl_S1, decl_S2, decl_com
36                write(102,*) cnt_time, HANGLE_S1, HANGLE_S2, h_com, gmu0_S1(
                      jhor), gmu0_S2(jhor), za_com
37             end if
38          end if
39       end if
40  end subroutine BINARY_Angles
```

Listing 8: Calculation of declination hour angle and zenith angle for each individual star.

```
1   subroutine BINARY_Distances(eccf,lamb)
2        use pumamod, only : N_DAYS_PER_YEAR, eccen, NROOT, mypid
3        use radmod, only : mvelpp
4        use BINARY_module
5
6        real :: eccf, lamb
7        real :: r
8        ! Distance Star-Planet
9        real :: S1P, S2P
10       ! Distance Star-Barycenter
11       real :: S1C, S2C
12
13       real :: occang = 0.02 ! Occultation angle in radians
14       real :: ve_rad
15       real :: tmp1, tmp2, tmp3
16       integer :: occul_cnt = 0
17       integer :: occul_thr = 100 ! Occultation can appear every 100. step
18
19       if (sel_bin.eq.1) then
20          ! Pass lambda to binary module
21          com_lamb = lamb
22
```

```
23          ! Set vernal equinox to 0, for sake of convenience
24          ve_rad = 0.
25
26          ! Compute planetary coordinates
27          r = sma*1./sqrt(eccf)
28          coor_P(1) = r*cos(lamb + ve_rad)
29          coor_P(2) = r*sin(lamb + ve_rad)
30
31          ! Compute Star-planet distances and eccentricity factors
32          S1P = sqrt((coor_P(1) - coor_S1(1))**2. + (coor_P(2) - coor_S1(2))
                **2.)
33          S2P = sqrt((coor_P(1) - coor_S2(1))**2. + (coor_P(2) - coor_S2(2))
                **2.)
34          eccf_S1 = (sma/S1P)**2.
35          eccf_S2 = (sma/S2P)**2.
36
37          ! Write output
38          cnt_time = cnt_time + 45./(60.*24.)
39          if (mypid.eq.NROOT) then
40             write(98,*) cnt_time, coor_S1(:), coor_S2(:), coor_P(:)
41             write(99,*) cnt_time, mvelpp, eccen, r, r2, com_lamb, S1P, S2P,
                    eccf, eccf_S1, eccf_S2
42          end if
43
44          ! Compute solar constant based on stars luminosity
45          if (switch_insol) then
46             gsol0_S1 = (L_S1*Lsolar)/(4.*pi*r**2.)
47             gsol0_S2 = (L_S2*Lsolar)/(4.*pi*r**2.)
48             switch_insol = .False.
49          end if
50
51          ! Compute angles relative to reference (x-axis)
52          angle_S1 = acos(coor_S1(1)/(sqrt(sum(coor_S1(:)**2.))))
53          angle_S2 = acos(coor_S2(1)/(sqrt(sum(coor_S2(:)**2.))))
54          angle_P = acos(coor_P(1) /(sqrt(sum(coor_P(:)**2.))))
55          if (coor_S1(2).lt.0.) angle_S1 = 2.*pi - angle_S1
56          if (coor_S2(2).lt.0.) angle_S2 = 2.*pi - angle_S2
57          if (coor_P(2) .lt.0.) angle_P = 2.*pi - angle_P
58
59          ! Compute star distances relative to COM
60          S1C = sqrt((coor_S1(1)-com(1))**2. + (coor_S1(2)-com(2))**2.)
61          S2C = sqrt((coor_S2(1)-com(1))**2. + (coor_S2(2)-com(2))**2.)
62
63          ! Compute apparent angle between star and COM
64          tmp1 = (r**2. + S1P**2. - S1C**2.)/(2.*r*S1P)
65          tmp2 = (r**2. + S2P**2. - S2C**2.)/(2.*r*S2P)
66          if (tmp1.gt.1.0) tmp1 = 1.0
67          if (tmp2.gt.1.0) tmp2 = 1.0
68          apS1C = acos(tmp1)
```

```
69          apS2C = acos(tmp2)
70
71          ! Compute occultation
72          occul_cnt = occul_cnt + 1
73          if (angle_P.gt.angle_S1-occang.and.angle_P.lt.angle_S1+occang.and.
                incl1.lt.incl_thresh_occul.and.occul_cnt.gt.occul_thr) then
74             occul_S2 = (A_S2 - A_S1)/A_S2
75             if (occul_S2.lt.0) occul_S2 = 0.
76             occul_cnt = 0
77          else if (angle_P.gt.angle_S2-occang.and.angle_P.lt.angle_S2+occang
                .and.incl1.lt.incl_thresh_occul.and.occul_cnt.gt.occul_thr)
                then
78             occul_S1 = (A_S1 - A_S2)/A_S1
79             if (occul_S1.lt.0) occul_S1 = 0.
80             occul_cnt = 0
81          else
82             occul_S2 = 1.
83             occul_S1 = 1.
84          end if
85
86          ! Compute signs for apparent angle
87          if (angle_S1.gt.angle_P-pi.and.angle_S1.lt.angle_P.or.angle_S1.gt.
                angle_P+pi) then
88             sign_S1 = -1
89             sign_S2 = +1
90          else
91             sign_S1 = +1
92             sign_S2 = -1
93          end if
94       end if
95  end subroutine BINARY_Distances
```

Listing 9: Computation of binary and planet coordinates as well as distances.

```
1   subroutine BINARY_Insolation(zftop1,zftop2,zsolar1,zsolar2,gsol0)
2        use BINARY_module
3        use pumamod, only : NROOT, mypid
4
5        real :: zsolar1, zsolar2, gol0
6        real :: insolation1, insolation2
7        real, dimension(NHOR) :: zftop1, zftop2
8        real, dimension(NHOR) :: zftop1_bin, zftop2_bin
9
10       ! Write output: insolation of each star
11       insolation1 = (zsolar1 + zsolar2) * gsol0_S1 * eccf_S1 * occul_S1
12       insolation2 = (zsolar1 + zsolar2) * gsol0_S2 * eccf_S2 * occul_S2
13       if (mypid.eq.NROOT) then
14         write(97,*) cnt_time, insolation1, insolation2, insolation1 +
               insolation2
15       end if
```

```
16
17       ! Total insolation per spectral partitioning
18       zftop1_bin = zsolar1 * (gsol0_S1 * eccf_S1 * occul_S1 * gmu0_S1 +
             gsol0_S2 * eccf_S2 * occul_S2 * gmu0_S2)
19       zftop2_bin = zsolar2 * (gsol0_S1 * eccf_S1 * occul_S1 * gmu0_S1 +
             gsol0_S2 * eccf_S2 * occul_S2 * gmu0_S2)
20
21       zftop1 = zftop1_bin
22       zftop2 = zftop2_bin
23   end subroutine BINARY_Insolation
```

Listing 10: Computation of the binary insolation.

```
1  &binary_nl
2  sel_bin = 1
3  Planet_SemiMajorAxis = 1.24
4  Binary_SemiMajorAxis = 0.176
5  Binary_Eccentricity = 0.0
6  Star1_SolarMass = 0.8094
7  Star2_SolarMass = 0.8877
8  sel_StefanBoltzmann = 1
9  R_S1 = 0.7861
10 R_S2 = 1.0284
11 Temp_S1 = 5202.
12 Temp_S2 = 5606.
13 dt = 225.0
14 /END
```

Listing 11: binary_namelist example